Hindawi
Geofluids
Volume 2021, Article ID 6611140, 22 pages
https://doi.org/10.1155/2021/6611140

Research Article

Genesis of Dolomite in Middle Permian Maokou Formation in Eastern Sichuan: Constraints from *In Situ* Geochemistry, Sr-Mg Isotopes, and Fluid Inclusions

Yanxia Jiang,[1,2] Xianfeng Tan,[3] Chengjiang Zhang,[1] Wei Jiang,[4] Jia Wang,[3] Long Luo,[3] Dongping Tan,[3] Wei Wang,[2] and Zhifu Xiong[2]

[1]*College of Earth Science, Chengdu University of Technology, Chengdu 610059, China*
[2]*Sinopec Exploration Company, Chengdu 610041, China*
[3]*Chongqing Key Laboratory of Complex Oil and Gas Exploration and Development, Chongqing 401331, China*
[4]*School of Earth Science and Engineering, Nanjing University, Nanjing 210046, China*

Correspondence should be addressed to Xianfeng Tan; xianfengtan8299@163.com

Received 26 October 2020; Revised 31 December 2020; Accepted 8 January 2021; Published 29 January 2021

Academic Editor: Kun Zhang

The dolostone reservoir of the Middle Permian Maokou Formation in Eastern Sichuan has good prospects for oil and gas exploration. Study of dolomitizing genesis of the Maokou Formation is essential for predicting the distribution of the dolostone reservoir. Petrography, *in situ* geochemistry, Sr-Mg isotopes, and fluid inclusions were carried out on samples from the Maokou Formation in Eastern Sichuan in order to discuss the dolomitizing process. Based on mineral and textural characteristics, dolomites were divided into four components: partially clouded dolomite (PCD), mosaic-like dolomite (MLD), cloudy-centered and clear-rimmed dolomite (CACD), and saddle dolomite (SDD). Results indicate that the Maokou Formation in Eastern Sichuan mainly experienced two stages of dolomitization. PCD, MLD, and cloudy-centered dolomite (CCD) were formed during the early dolomitization. They all show turbid crystal planes and bright orange-red CL and have similar trace element contents, $^{87}Sr/^{86}Sr$ ratios, and rare-earth patterns, indicating that they might be formed in the same fluid. This is a period when dolomitizing fluids mainly migrated along pores or microcracks and replaced protogenetic calcites, which occurred in the shallow burial stage of the Maokou Formation before the Late Permian. Clear-rimmed dolomite (CRD) and SDD were formed in the late stage of dolomitization. They all have clean crystal planes and darkly red CL. CRD of the ERY profile has trace element contents, $^{87}Sr/^{86}Sr$ ratios, and rare-earth patterns similar to SDD of the HLCH profile and Well TL6, inferring that both may be formed in the same fluid. Combined with high SrO contents and homogenous temperatures of fluid inclusions of CRD and SDD and Mg-isotopic compositions, they were generated by hydrothermal dolomitization. The hydrothermal fluid stage is related to the movement of the Emeishan Large Igneous Province, which was made up of basaltic magmatic fluids mixing with the surface water. The hydrothermal fluid mainly migrated upwards along structural fractures or faults and filled in structural fractures, occurring in the Late Permian to Middle-Late Triassic.

1. Introduction

The genesis of dolomite has been a perplexing problem for geologists [1]. Over the past two hundred years, many dolomitizing models have been proposed, such as the sabha model, the seepage-reflux model, the evaporative-pump model, the mixed-water model, and the microbial exchange model [2–7]. In the past two decades, more and more geologists paid attention to the hydrothermal dolomitization model due to lots of reports of deeply buried dolostones [8–10]. For instance, Niu et al. [11] argued that the Lower Ordovician dolomite in the southwest Tarim Basin was dolomitized by hydrothermal fluids mainly migrating along the fracture system. Nevertheless, hydrothermal dolostones are products of the multistage dolomitization and may have undergone complicated diagenetic processes [12–14]. Therefore, it is

very difficult to accurately identify sources and properties of hydrothermal fluids. Nonetheless, geochemistry and stable isotope composition of carbonate minerals or rocks are closely associated to the diagenetic environment and provide important information regarding paleosalinity, paleotemperature, and paleoclimate. Therefore, the composition of stable isotopes is of great significance to the diagenetic environment of carbonate rocks, and is also important for distinguishing the genesis of dolomite [15–18]. And distribution of major and trace elements in strata reflects changes of the diagenetic environment to a certain extent [19–22].

In Eastern Sichuan, a 23-meter-thick dolostone reservoir of the Maokou Formation was discovered in Well TL6 with a daily output of about $11.08 \times 10^4\ m^3$ industrial gas flow obtained, indicating that the dolostone reservoir in the Maokou Formation in Eastern Sichuan has good prospects for oil and gas exploration [23]. Understanding the dolomitizing mechanism is essential for predicting the spatial distribution of the dolostone reservoir in the Maokou Formation in Eastern Sichuan. The dolomite development zone of the Maokou Formation in Eastern Sichuan is extended towards to the NW-SE direction and overlaps with the No. 15 basement fault belt in the geographic space (Figure 1(b)). Thus, some scholars proposed that hydrothermal fluids generated by the Emei taphrogeny are the main factor for forming dolomites of the Maokou Formation in Eastern Sichuan [23–26]. For example, Zhang et al. [24] argued that the saddle-shaped dolomite and matrix dolomite of the Maokou Formation filling in the pores and fractures in Eastern Sichuan were formed by contemporaneous multistage hydrothermal fluids altering protogenetic calcites. Nonetheless, distinct dolomitizing genetic models have also been proposed by different scholars including the burial model [27], the mixed-water model [28], and the hot-water model [29–31]. Previous studies were mainly based on a single field profile, petrography or bulk-rock geochemistry, and fluid inclusion, whereas they lack comprehensive evidence from various aspects and demonstration from *in situ* geochemistry. Consequently, by integrating multiple field profiles, *in situ* geochemistry, Sr-Mg isotopes, and fluid inclusions, this study is able to discuss in detail dolomitizing stages, Mg^{2+} sources, dolomitizing time, models, and lateral differences of the Middle Permian Maokou Formation in Eastern Sichuan, which enables providing references for predicting the distribution of the dolostone reservoir.

2. Geological Settings

2.1. Structural Background. The study area has the domian of$26 \times 10^3\ km^2$and is located on the eastern part of Sichuan Basin and belongs to the high-steep structural zone in Eastern Sichuan, close to the Huayingshan fault zone and the Daba Mountain [32] (Figure 1(a)). Basement rocks are composed of Archean intermediate-basic rocks and Proterozoic gneisses, developing two sets of basement faults in NE and NW directions [33] (Figure 1(b)). Eastern Sichuan experienced multitectonic cycles in geological history. Since the Maokou Period, Eastern Sichuan has undergone the Tungwu Movement and the Yanshan-Himalaya Movement, and the tectonic environment has successively transformed from a rift basin and an intracontinental depression basin to the Huayingshan high-steep structural belt [34]. Sichuan Basin was dominated by a gentle-slope carbonate platform facies in the Maokou Period [35]. The Emei taphrogeny caused dispersion of the carbonate platform, the crustal extension, and differential uplift of fault blocks in the middle-upper Yangtze region and facilitated reactivating basement faults [36, 37].

2.2. Stratigraphic and Sedimentary Background. The Kaijiang-Liangping area rapidly sank to form a relatively deep-water environment affected by the Tungwu Movement which was an outside gentle-slope facies. The Tailai area belonged to a middle gentle-slope facies with extensively contiguous bioclastic beaches [23]. Hence, the main body of the Maokou Formation in Eastern Sichuan is a set of marine carbonate rocks which was weakly influenced by terrigenous materials. At present, the thickness of the residual strata of the Maokou Formation ranges from 90 to 400 m; the thicker locations are mainly concentrated at southwest and northwest Sichuan, and the strata gradually becomes thinner towards the northeast [26] (Figure 1(b)). The Maokou Formation in Eastern Sichuan is divided into three members from bottom to top. Member 1 consists of dark-gray augen limestone and grey-black micritic limestone (Figure 2). Thin-layered and lenticular siliceous rocks containing a large number of chert nodules are developed in Member 1 (Figure 2). The calcareous shales exist in the lower part of Member 1, interlaying between augen limestones and siliceous rocks (Figure 2). Member 2 is made up of dark-gray micrite bioclastic limestones and granular limestones (Figure 2). Member 3 is composed of dolostone, siliceous dolostone, and bioclastic limestone. The top is eroded and bauxite mudstones are developed, showing parallel unconformity contact with the overlying Wujiaping Formation or Longtan Formation (Figures 2 and 3(a)). Fine-grained dolostones and siliceous rocks contain multiple mineral assemblages related to hydrothermal fluids, such as microcrystallized quartz+dolomite, saddle dolomite+megacrystalline calcite, coarse-grained dolomite+calcite+sphalerite, and pyrite+marcasite.

3. Analytic Methods

3.1. Sampling. In order to discuss the lateral changes of dolomitization in the Middle Permian Maokou Formation, samples were collected from the ERY profile, the HLCH profile, and Well TL6 (Figure 2). The three profiles extend along the NW-SE direction, consistent with the distribution of dolostones in the Maokou Formation (Figure 1(b)). A total of 25 samples were collected (Figure 2). The strata involve Member 1 and Member 3, including dolomites and limestones. To guarantee the accuracy of analytic results, the collected samples are all fresh and organic poor. All samples are equipped with thin sections, and typical samples are selected for *in situ* geochemistry and Sr-Mg isotope analyses. Analyses of *in situ* major and trace elements, *in situ* Sr isotope, and single mineral solution Mg isotope were carried out at the State Key Laboratory of Continental Dynamics at Northwest University.

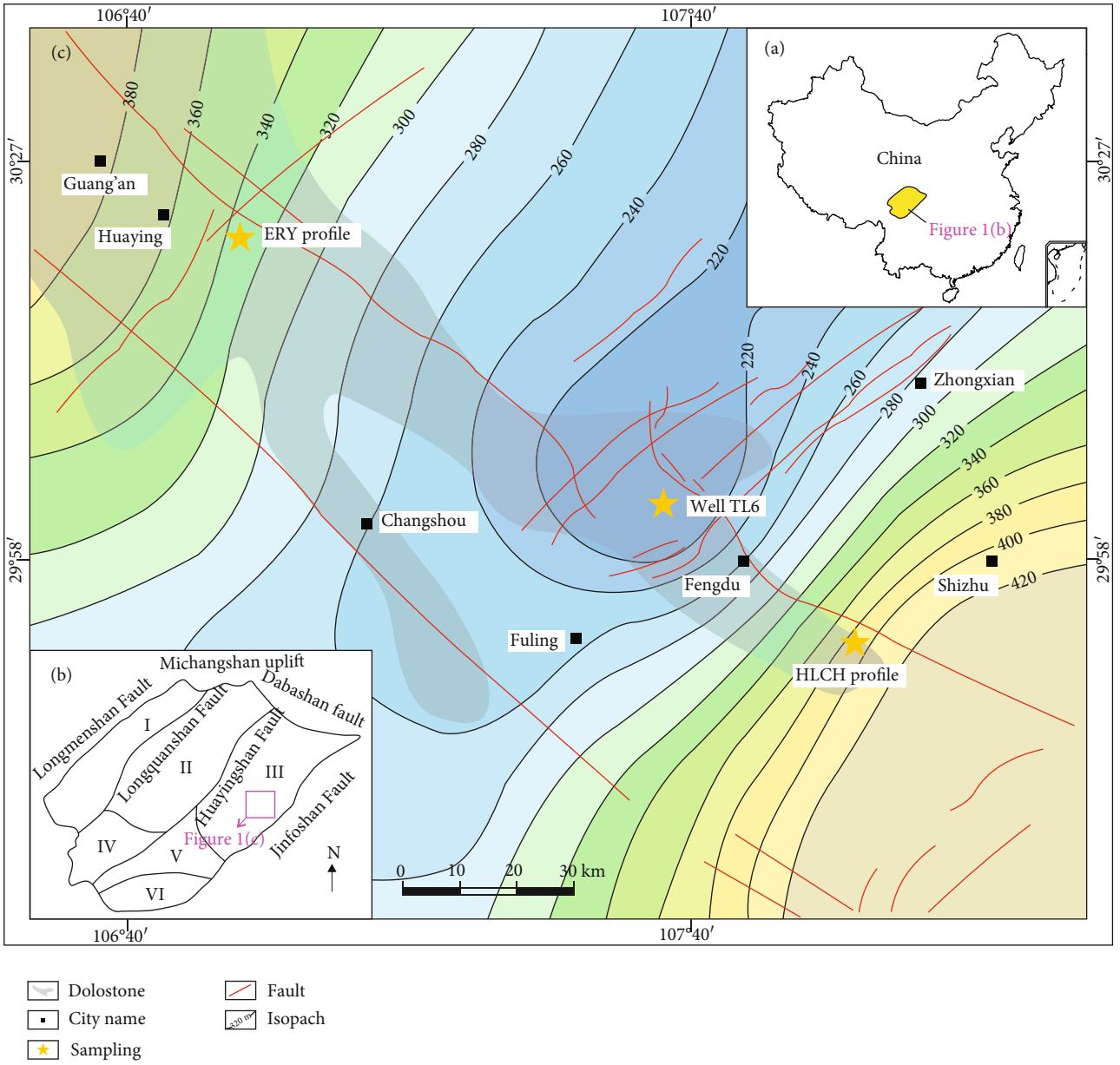

FIGURE 1: (a) Location of the Sichuan Basin in Chinese territory. (b) Geographic location of the study area in Eastern Sichuan. (c) Locations of sampling profiles [34]. I—structural zone in Western Sichuan; II—structural zone in Central Sichuan; III—structural zone in Eastern Sichuan; IV—structural zone in Southwestern Sichuan; V—structural zone in Southern Sichuan; VI—structural area of Sichuan-Yunnan-Guizhou.

3.2. Major Elements. Analyses of major elements of different minerals were carried out at the State Key Laboratory of Continental Dynamics at Northwest University. The *in situ* major elements are detected with the JXA-8230 electron probe produced by JEOL. The experimental electron beam acceleration voltage is 15 kV, the current is 10 nA, and the electron beam spot diameter is 2~5 μm.

3.3. Trace Elements. Analyses of trace elements of different minerals were carried out at the State Key Laboratory of Continental Dynamics at Northwest University. LA-ICP-MS was used for *in situ* trace element analyses. The ICP-MS used was the GeoLas Pro produced by Coherent Lambda Physik, and the LA used was Agilent 7500a produced by Agilent, with an average power of 4 W and a beam spot diameter of 32 μm.

3.4. Sr-Mg Isotopes. Analyses of *in situ* Sr isotope and solution Mg isotope for minerals were carried out at the State Key Laboratory of Continental Dynamics at Northwest University. *In situ* Sr isotope and solution Mg isotope detection adopted the Nu Plasma II multicollector inductively coupled plasma mass spectrometer (MC-LA-ICP-MS) produced by the Nu Company in the United Kingdom. Standard samples are seawater, BHVO-2, and BCR-2. The quality inspection process is to test the standard sample and the sample 3 times, respectively, referring to Yuan [38] for the detailed analysis process.

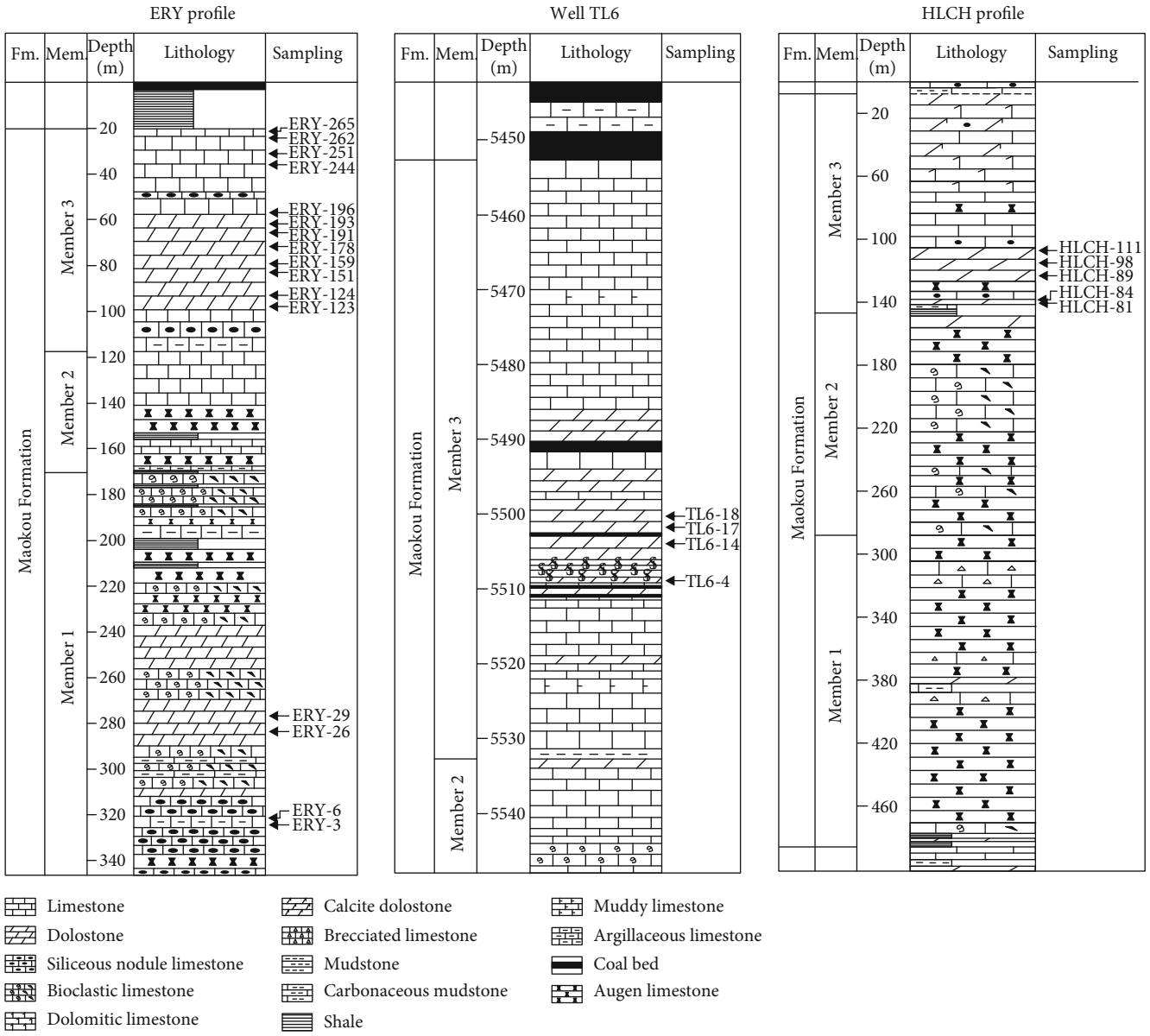

Figure 2: The comprehensive stratigraphic columns showing lithology and sampling sites of the Maokou Formation.

3.5. Cathodoluminescence and Fluid Inclusions. Analyses of cathodoluminescence (CL) and homogenous temperatures of fluid inclusions were completed at the Experimental Inspection Center of Xi'an Institute of Geology and Mineral Resources. CL detection uses the CL8200MK5 CL microscope with a 12~15 kV beam and a current intensity of 420~430 mA on the nonstained halves of thin sections. Homogenous temperatures of fluid inclusions were measured by the THMSG 600 geological inclusion measurement system, which is composed of geological cold and hot stage and polarizing microscope with a range of -196°C to 600°C. Homogenization temperatures using the equation of Bodnar in 1993 in terms of the H_2O-NaCl system were measured with a precision (reproducibility) of ±1. To limit the possibility of measuring deformed aqueous inclusions, only primary inclusions from the same field of view were measured during a single heating or freezing run. Heating runs were conducted before freezing runs to reduce the possibility of inclusion stretching by freezing.

4. Results

4.1. Petrographic Features

4.1.1. Petrology

(1) Limestone. Limestones include augen limestone (Figure 3(b)), micrite limestone, spherulitic limestone, bioclastic limestone (Figure 3(c)), conglomerate limestone (Figure 3(d)), dolomite limestone (Figure 3(e)), chert nodule limestone (Figure 3(f)), breccia limestone, and argillaceous limestone. The bottom of the Maokou Formation is dominated

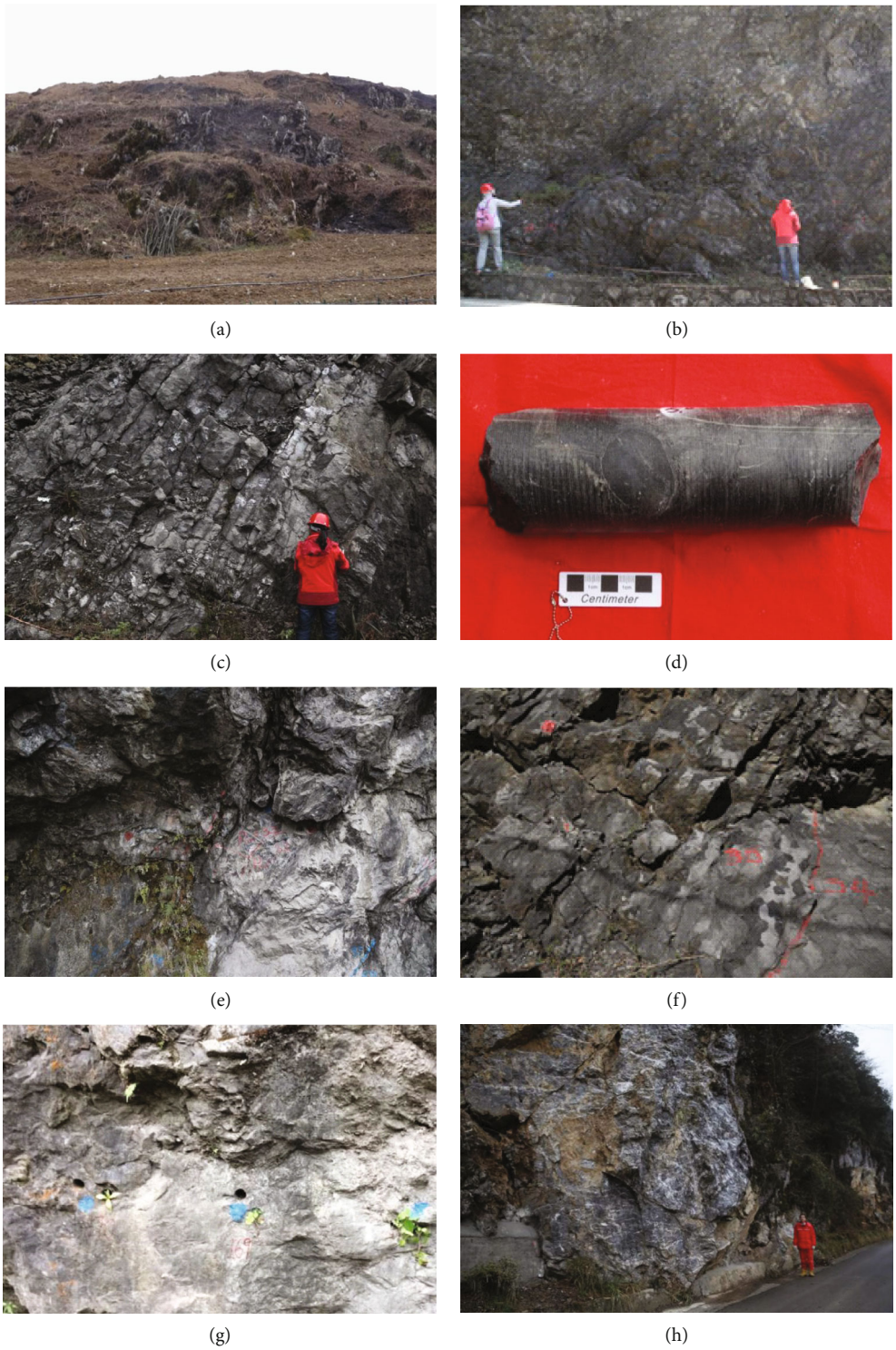

(a) (b) (c) (d) (e) (f) (g) (h)

Figure 3: Continued.

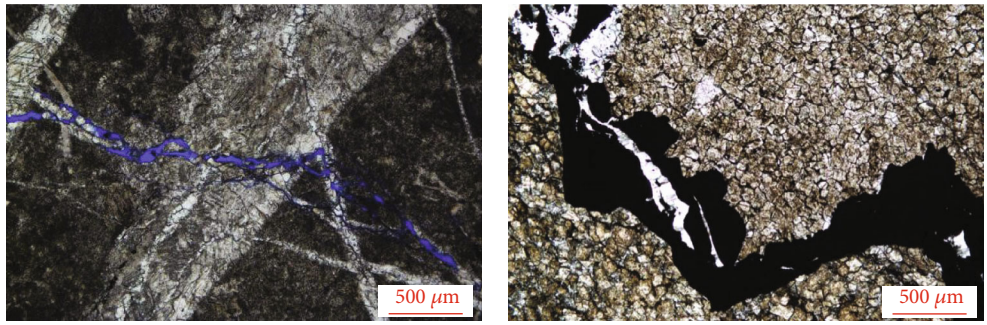

(i) (j)

Figure 3: (a) Karst limestone; on top of Member 3 of the Maokou Formation in the HLCH profile. (b) Darkly grey augen limestone; Member 2 of the Maokou Formation in the HLCH profile. (c) Dolomite-bearing bioclastic limestone; Member 2 of the Maokou Formation in the ERY profile. (d) Gravel limestone; Well TL6. (e) Nubby dolomitic limestone; Member 2 of the Maokou Formation in the ERY profile. (f) Paramoudras-bearing bioclastic limestone; Member 2 of the Maokou Formation in the HLCH profile. (g) Fine-grained dolostone; Member 3 of the Maokou Formation in the ERY profile. (h) Reticulate carbonate veins; Member 3 of the Maokou Formation in the HLCH profile. (i) Two phases of carbonate veins in the HLCH profile. (j) Residual hydrocarbons in carbonate veins; Well TL6.

by dark-gray micrite limestones and spherulitic limestones and transforms upwards into sparry bioclastic limestones. Bioclastic limestones occurred in Member 2 containing few organic matter, namely, Crinoidea and Textulariina. Dolomitized limestones exist in each member of the Maokou Formation with partially clouded characteristics and dolomite contents < 40%. Dolomite-bearing limestones are distributed in Member 1 with dolomite contents < 10%. Bioclastic spherulitic limestones were developed anywhere. Their matrix contains fine veins and leaching dissolved pores of about 2%. Sparry biospherulitic limestones are distributed on top of Member 3, containing fusulinid and carbonate veins. Dissolved pores are commonly filled by calcite.

(2) Dolostone. Dolostones are the most important type of Member 3 and the dominating reservoir in the study area. Rock types include fine-grained dolomite, siliceous dolomite, and calcilized dolomite. Both the ERY and HLCH profiles have undergone different degrees of dolomitization from Member 1 to Member 3. Member 1 and Member 2 only developed lamellar fine-grained dolomite, while Member 3 developed thickened middle-grained dolomite (Figure 3(g)). Less dolostones contain a small amount of residual biological debris located at the boundary between Member 1 and Member 2. And the dolomite has an anhedral shape. Both drilling cores and field profiles developed netted fractures and were filled by carbonate veins (Figure 3(h)). There are at least two stages of carbonate veins. Field and microscope observations show that the second-stage carbonate veins cut the first-stage carbonate veins off (Figure 3(i)). Residual hydrocarbons filling in the carbonate veins can be observed (Figure 3(j)).

4.1.2. Textural Components of Dolomite. According to the microscopic characteristics of drilling cores and field samples, dolomites with granular texture can be divided into four components on the basis of clouding degree, microtexture, CL, and geochemical compositions: partially clouded dolomite, cloudy-centered and clear-rimmed dolomite, mosaic-like dolomite, and saddle dolomite, respectively.

(1) Partially Clouded Dolomite. Partially clouded dolomite (PCD) is mainly a fine-silty crystal with a subhedral-euhedral texture. The crystal plane is turbid and colorless or light yellow-brown. They are scattered in the matrix, and the original texture is still clear (Figure 4(a)). Moreover, they are the main components of micrite bioclastic limestones or sprite bioclastic limestones, which are predominately distributed in Member 1 and Member 2. The CL is brightly orange-red (Figure 4(b)), different from the dark-red calcite core. Under the BSE (backscattered electron) condition, partial dolomitization can obviously be seen (Figure 5(a)). The residual protogenetic calcite is mottled and is distributed in the dolomite rim and core.

(2) Cloudy-Centered and Clear-Rimmed Dolomite. Cloudy-centered and clear-rimmed dolomite (CACD) is mainly a fine-medium crystal with a euhedral texture and mainly occurs in fine-grained dolostones. Its core has a turbid crystal plane, and its edge has a clean crystal plane, with a typically cloudy-centered and clear-rimmed texture (Figure 4(c)), which is one of the main components of Member 3. The CL of clear-rimmed dolomite (CRD) is darkly orange-red, and the CL of cloudy-centered dolomite (CCD) is brightly orange-red (Figure 4(d)). The turbid crystal plane of CCD is still clear under the BSE condition, and the core-rim texture is exhibited visibly in contrast with CRD (Figure 5(c)).

(3) Mosaic-Like Dolomite. Mosaic-like dolomite (MLD) is a fine-silty crystal with a subhedral-anhedral and equigranular or inequigranular texture and is mainly found in fine-grained dolostones. They are in close contact with each other with turbid and yellowish brown crystal planes (Figure 4(e)). Furthermore, it is one of the main components of Member 3. The CL is brightly orange-red (Figure 4(f)). A turbid crystal plane can be seen likewise under the BSE condition (Figure 5(b)).

(4) Saddle Dolomite. Saddle dolomite (SDD) develops in the carbonate veins (Figure 4(g)). It is dominated by a medium-coarse grain, some of which is curved and fills in

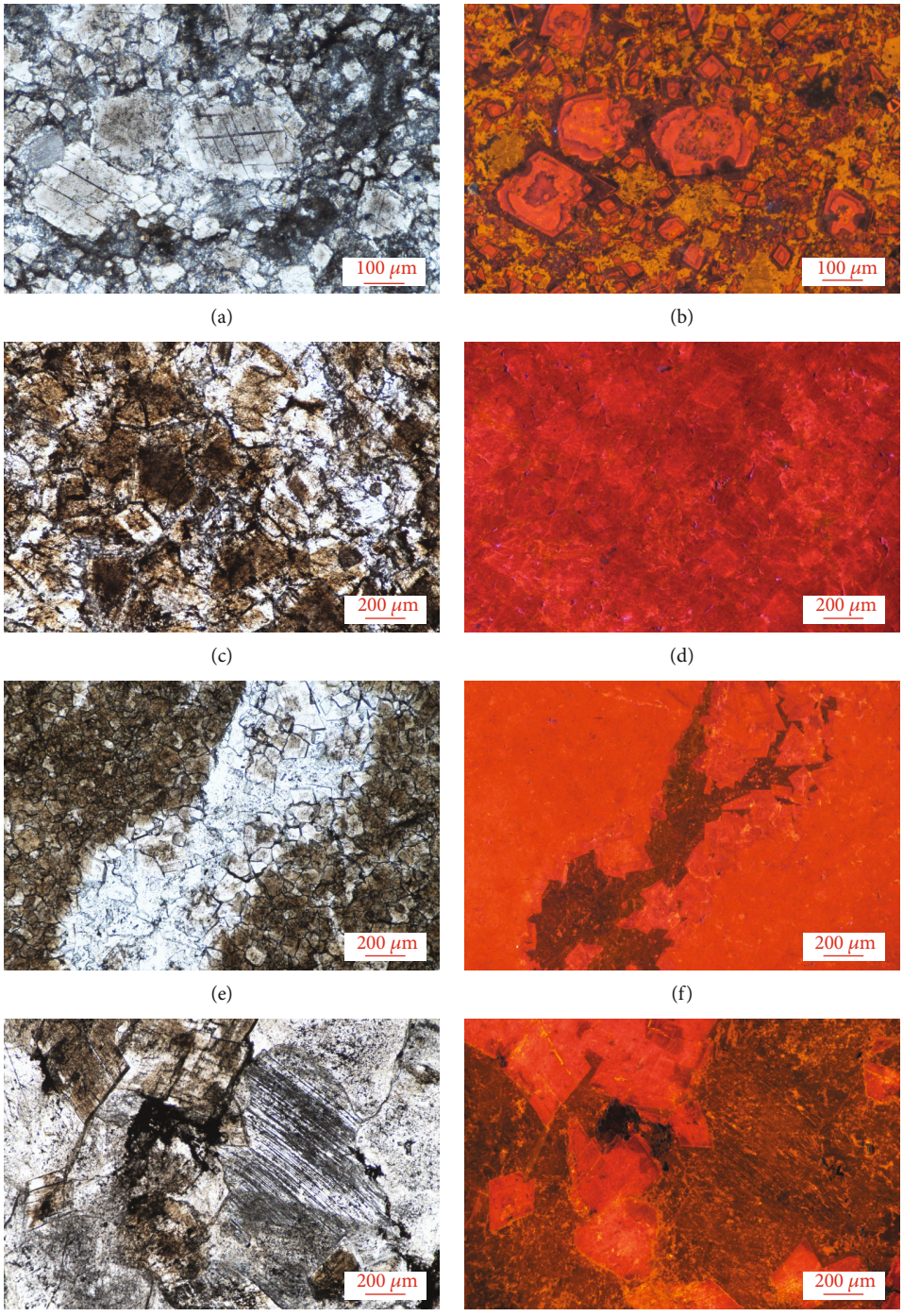

Figure 4: (a) PCD reserves the texture of protogenetic calcite in the HLCH profile. (b) PCD shows brightly orange-red CL in the HLCH profile. (c) CACD in the ERY profile. (d) CCD shows brightly orange-red CL, but CRD shows darkly red CL in the ERY profile. (e) MLD and carbonate vein with coarse-grained calcite in the core and SDD in the rim in the HLCH profile. (f) MLD shows brightly orange-red CL and SDD shows darkly red CL, but CGC is colorless in the HLCH profile. (g) CGC and SDD in the HLCH profile. (h) SDD shows darkly red CL, but CGC is colorless in the HLCH profile.

tensile structural fractures (Figure 4(e)). Carbonate veins are composed of coarse-grained calcite (CGC) and SDD. The vein wall is SDD, and the vein center is CGC (Figure 4(e)). The CL of SDD shows a darkly orange-red color (Figures 4(f) and 4(h)), different from MLD. Under the BSE condition, the crystal plane is still clean and in linear contact with the CGC (Figure 5(d)).

4.2. Major Elements. Different dolomite components have clear compositional zoning and geochemical differences

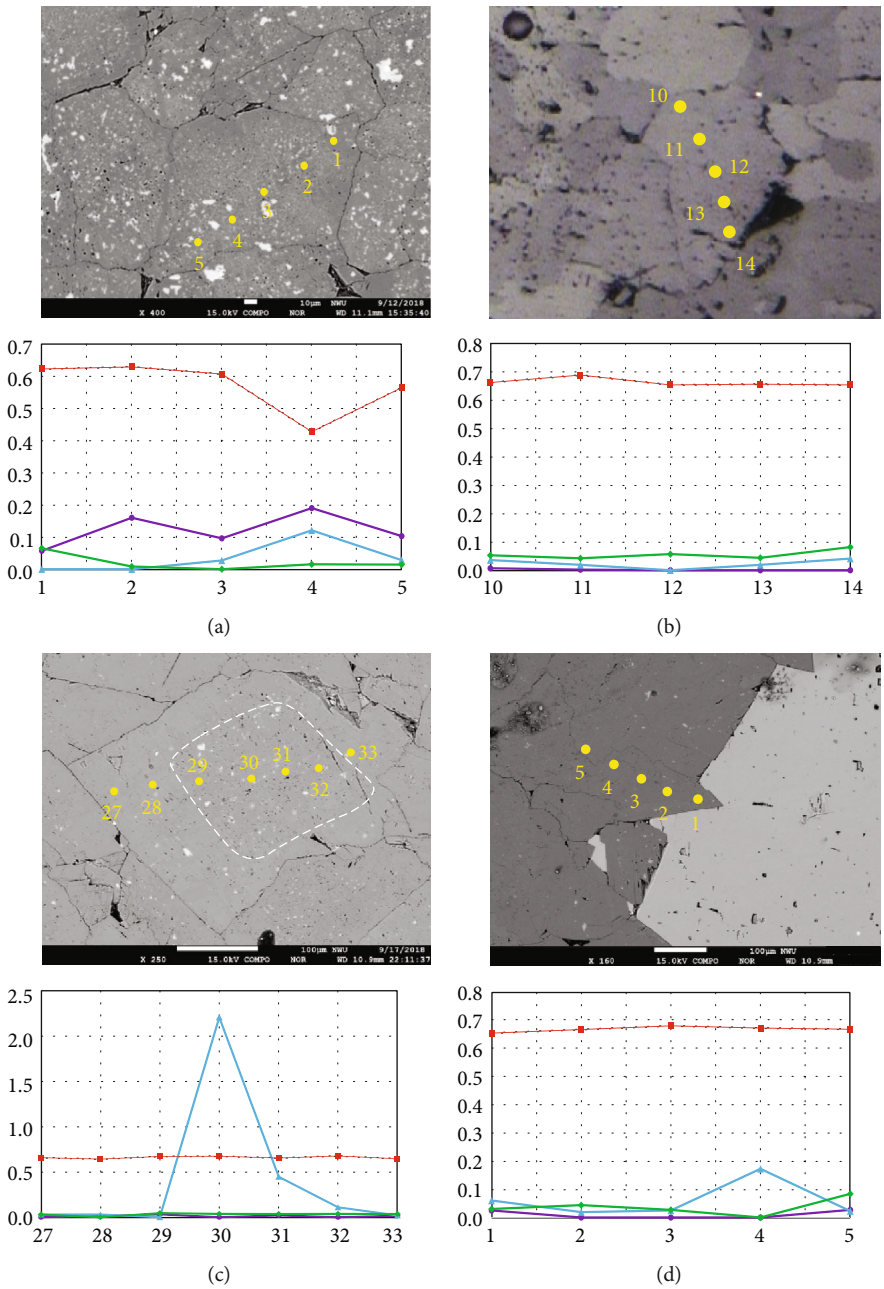

Figure 5: Continued.

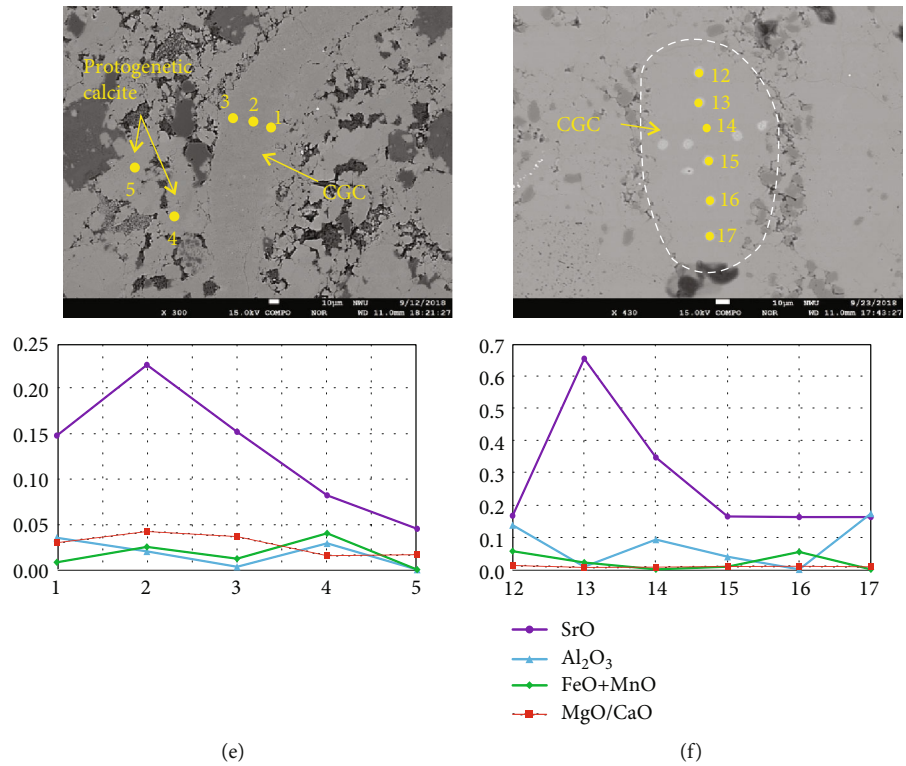

Figure 5: (a) Partially clouded dolomite in the BSE and ERY-3 profiles. (b) Mosaic-like dolomite in the BSE and HLCH-89 profiles. (c) Cloudy-centered and clear-rimmed dolomite in the BSE and ERY-151 profiles. (d) Saddle dolomite in the BSE and HLCH-98 profiles. (e) CGC and protogenetic calcite in the BSE and ERY-6 profiles. (f) CGC in the BSE and ERY-29 profiles. CGC: coarse-grained calcite.

(Figure 5). The MgO/CaO ratios of PCD show large variations. Where there are more protogenetic calcite residues, MgO/CaO ratios are significantly low corresponding to high Al_2O_3 contents. SrO contents progressively decrease from core to rim, whereas FeO+MnO contents did not change considerably (Figure 5(a)). MLD has no obvious changes in MgO/CaO ratios and Al_2O_3, SrO, and FeO+MnO contents. But the Al_2O_3, SrO, and FeO+MnO contents of MLD are lower than those of PCD, and the MgO/CaO ratios are higher than PCD (Figure 5(b)). The MgO/CaO ratios and SrO and FeO+MnO contents of CCD and CRD have no apparent variations, but their Al_2O_3 contents show a large change and a gradual decrease from core to rim (Figure 5(c)). The MgO/CaO ratios of CCD and CRD are between those of PCD and MLD, while the SrO and FeO+MnO contents of the former are lower than the latter. The MgO/CaO ratios of SDD did not vary markedly, whereas its core has higher Al_2O_3 but lower SrO and FeO+MnO contents than those of the rim (Figure 5(d)). The Al_2O_3, SrO, and FeO+MnO contents of the rim of SDD are analogous to protogenetic calcite (Figure 5(e)). By contrast, the CGC in the vein core has the characteristics of high SrO, low Al_2O_3, and FeO+MnO contents (Figures 5(e) and 5(f)), while the surrounding protogenetic calcite shows relatively higher Al_2O_3 and FeO+MnO and lower SrO contents and MgO/CaO ratios (Figure 5(e)).

4.3. Trace Elements. According to trace element compositions of different dolomite components, the same component has a large range of Sr, Ba, Na, Fe, and Mn contents and Rb/Sr ratios. MLD has Sr values of 45.15~843.3 ppm (parts per million; denoting concentration), Ba values of 0.39~99.91 ppm, and Rb/Sr ratios of 0.38~1039. The Fe+Mn and Na contents of MLD show a positive correlation with Rb/Sr ratios (Figures 6(b)–6(d)). CCD contains Rb/Sr values of 31.5~128 and Na contents of 553~4011 ppm (Figure 6(b)). CRD has Na and Fe+Mn contents of 488~527 ppm and 151~215 ppm and Rb/Sr values of 35.5~90.4, respectively. Both CCD and CRD show a positive correlation between Fe+Mn and Rb/Sr (Figure 6(e)). The Na contents of CCD are positively correlated with Rb/Sr ratios, but those of CRD are reversed (Figures 6(b) and 6(c)). SDD has Na, Sr, and Fe+Mn contents of 27.1~360 ppm, 42.3~840 ppm, and 54~850 ppm, respectively (Figures 6(c), 6(e), and 6(g)). The Sr contents of CGC show a significant variation from 66.2 to 1123 ppm, and its Na contents range from 1.42 to 139 ppm (Figures 6(c) and 6(g)). MLD of the HLCH profile contains lower Sr but higher Fe+Mn and Na contents and Rb/Sr ratios than those of the ERY profile (Figures 6(b)–6(e)). The Sr contents of SDD in the HLCH profile and Well TL6 are lower than those of the ERY profile (Figure 6(g)). The Fe+Mn contents of SDD in the HLCH and ERY profiles are lower than those of Well TL6 (Figure 6(e)). Nonetheless, the Ni+Co contents and Rb/Sr values of Well TL6 are similar to those of the HLCH and ERY profiles (Figure 6(h)).

Under the normalized condition of the post-Archean Australian shale (PAAS), all dolomite components show weakly depleted LREE and HREE but slightly enriched

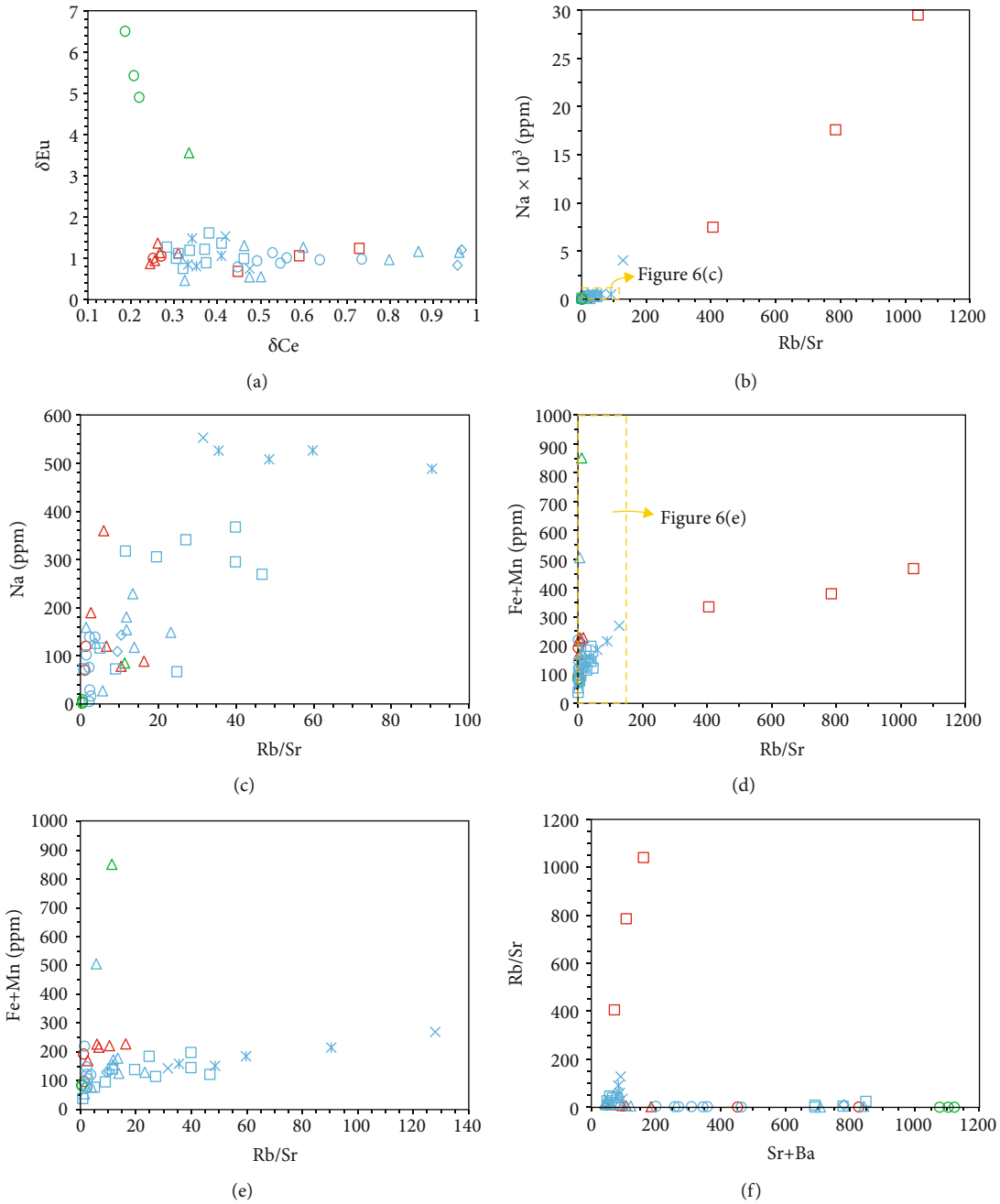

Figure 6: Continued.

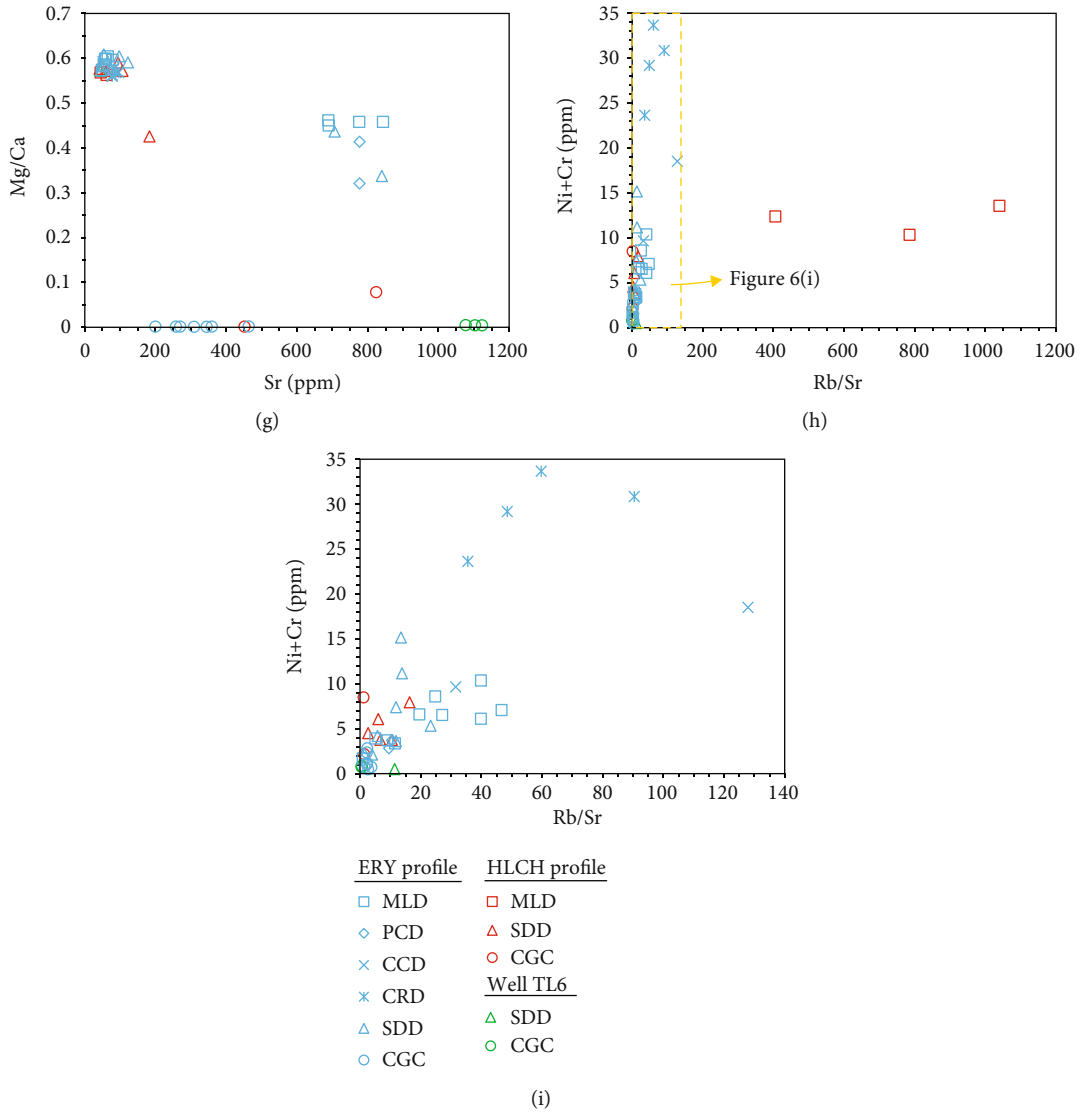

Figure 6: Binary diagrams of trace elements and ratios. PCD: partially clouded dolomite. MLD: mosaic-like dolomite. CCD: cloudy-centered dolomite. CRD: clear-rimmed dolomite. SDD: saddle dolomite. CGC: coarse-grained calcite.

MREE (Figure 7). Compared with the HLCH and ERY profiles, SDD and CGC in Well TL6 show obviously positive Eu anomalies and negative Ce anomalies, but CGC in Well TL6 displays more intensely depleted HREE (Figure 7(e)). MLD has higher total rare-earth contents (ΣREE) than SDD in the HLCH profile (Figure 7(c)). MLD has lower ΣREE than SDD in the ERY profile (Figure 7(a)). CGC of different profiles contains higher ΣREE (Figure 7). Under the normalized condition of the upper continental crust (UCC), spider diagrams of all dolomite components show U, La, Sr, and Y enrichment and Nb, Pb, and Ti depletion (Figure 7). MLD of the HLCH profile is enriched in Rb, Ba, Zr, and Hf, distinct from other components (Figure 7(d)).

4.4. Sr-Mg Isotopes. In this study, 7 samples were selected for *in situ* Sr isotope analyses of dolomite. The $^{87}Sr/^{86}Sr$ values of SDD in the HLCH profile range from 0.707864 to 0.715535 with an average value of 0.710378 (Figure 8(a)). PCD in the ERY profile has $^{87}Sr/^{86}Sr$ values of 0.707407~0.708054 with an average value of 0.707631 (Figure 8(a)). MLD in the ERY profile has $^{87}Sr/^{86}Sr$ values ranging from 0.707406 to 0.707605 with an average value of 0.707544 (Figure 8(a)). The $^{87}Sr/^{86}Sr$ values of CRD in the ERY profile range from 0.708095 to 0.712091 with an average value of 0.709482 (Figure 8(a)). CCD of the ERY profile has $^{87}Sr/^{86}Sr$ values of 0.707503~0.707808 with an average value of 0.707682 (Figure 8(a)). SDD of Well TL6 contains $^{87}Sr/^{86}Sr$ values ranging from 0.708060 to 0.708062 with an average value of 0.708061 (Figure 8(a)). The $^{87}Sr/^{86}Sr$ values of CGC in Well TL6 range from 0.708024 to 0.709714 with an average value of 0.708715 (Figure 8(a)).

A total of 4 single mineral samples were selected for solution Mg isotope analyses. The reference values of the standard samples are $\delta^{26}Mg_{BHVO-2} = -0.20 \pm 0.07‰$ and $\delta^{26}Mg_{SW} = -0.83 \pm 0.09‰$, which are all within the error range. The $\delta^{25}Mg_{\text{-DSM}}$ and $\delta^{26}Mg_{\text{-DSM}}$ values of all samples

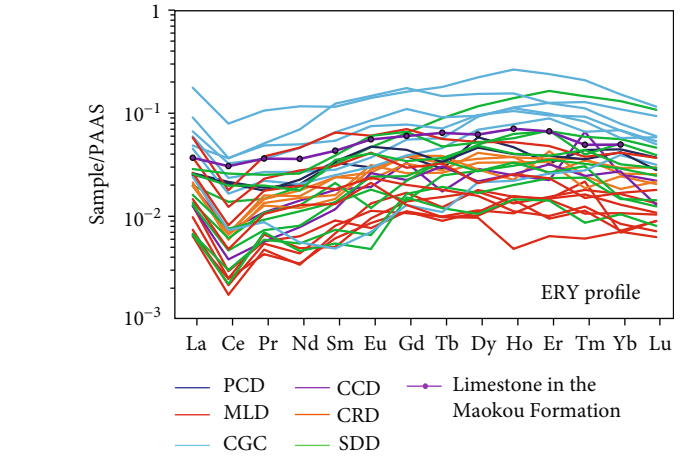

(a)

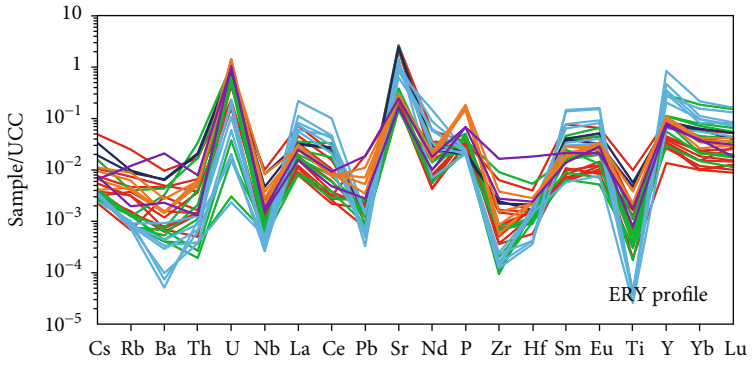

(b)

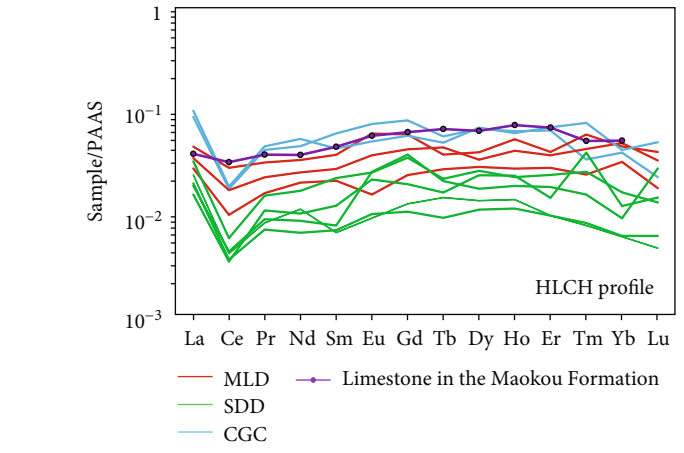

(c)

Figure 7: Continued.

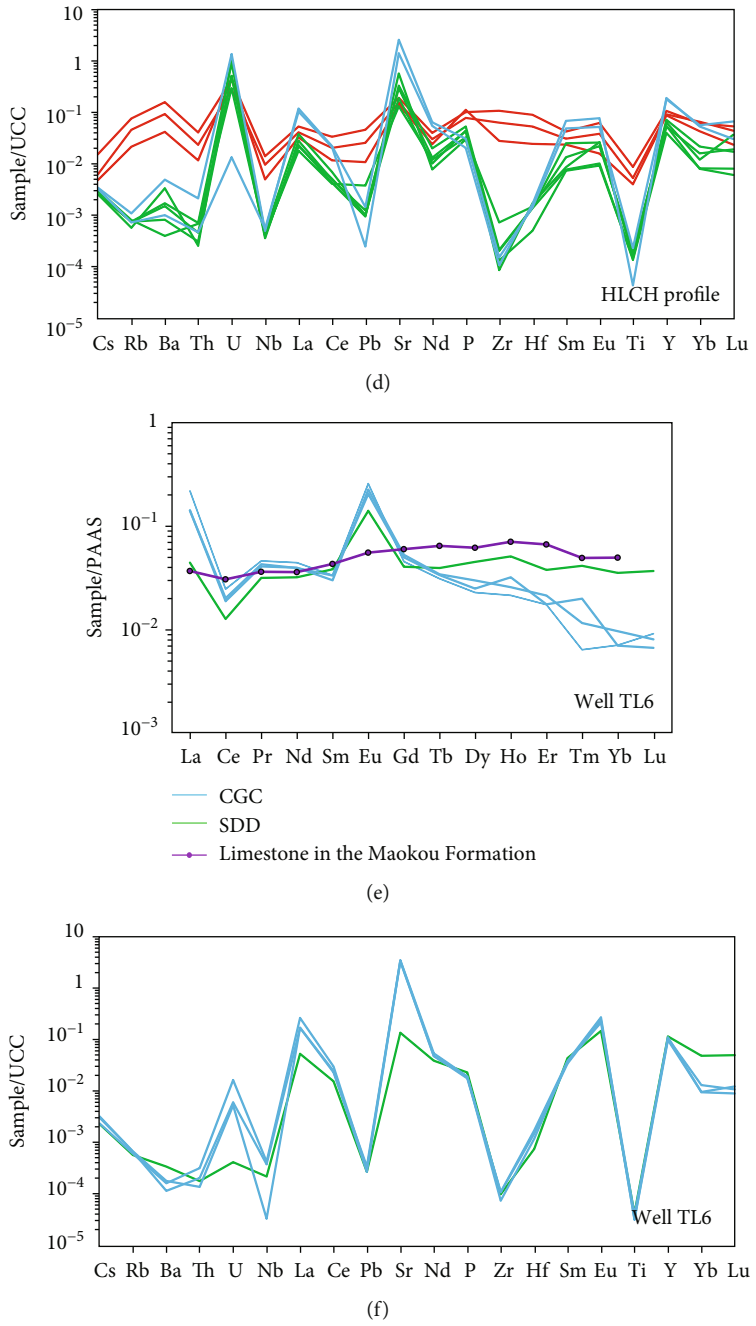

Figure 7: Post-Archean Australian Shale- (PAAS-) normalized rare-earth element (REE) patterns and Upper Continental Crust- (UCC-) normalized trace element spidergrams. The limestone in the Maokou Formation was from Li et al. [41]. PAAS data were from Mclennan et al. [62]. UCC data were from Rudnick and Gao [63].

fall on the mass fractionation line well (Figure 8(b)), indicating that the homoisotope interference can be ignored during the mass spectrometry analysis. PCD of the ERY profile has the lightest $\delta^{26}Mg_{\text{-DSM}}$ ranging from -3.43‰ to -3.41‰ (Figure 8(b)). The $\delta^{26}Mg_{\text{-DSM}}$ values of SDD in the ERY profile are -1.51‰~-1.43‰ (Figure 8(b)). SDD in the HLCH profile has $\delta^{26}Mg_{\text{-DSM}}$ values of -2.20‰~-1.53‰ (Figure 8(b)). The $\delta^{26}Mg_{\text{-DSM}}$ values of SDD in Well TL6 is -1.02‰. The $\delta^{26}Mg_{\text{-DSM}}$ values of PCD are significantly lower than that of SDD (Figure 8(b)).

4.5. Homogenous Temperature of Fluid Inclusions. Crystallization temperatures of different dolomite components can be referred to based on the homogenization temperature of fluid inclusion. Due to the influence of fluid density and viscosity, there are relatively more fluid inclusions in SDD than other components (Figure 9(a)). The fluid inclusion in CCD is rectangular in shape and has an isolated protogenetic brine inclusion (Figure 9(b)). Because it is difficult to find fluid inclusions in CCD, the unique homogenous temperature measured is 57.4°C (Figure 10). Fluid inclusions in CRD are

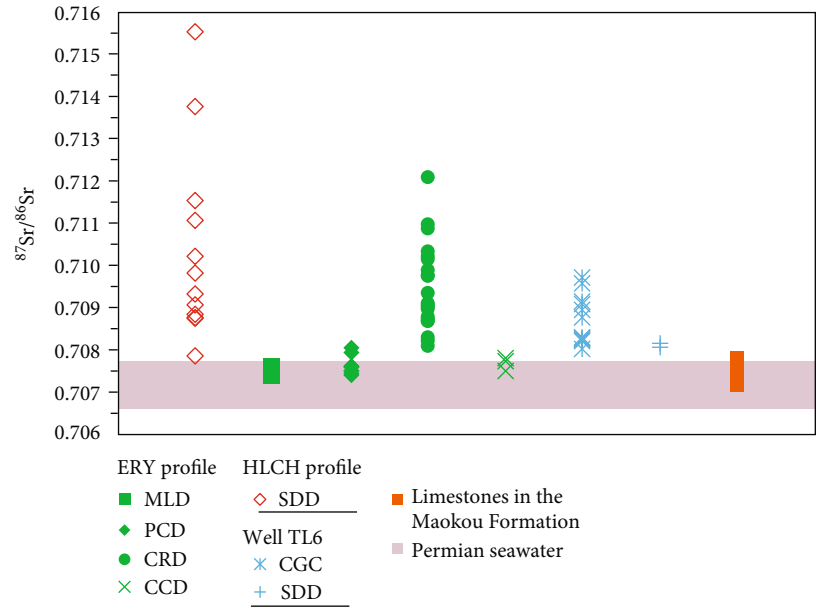

(a)

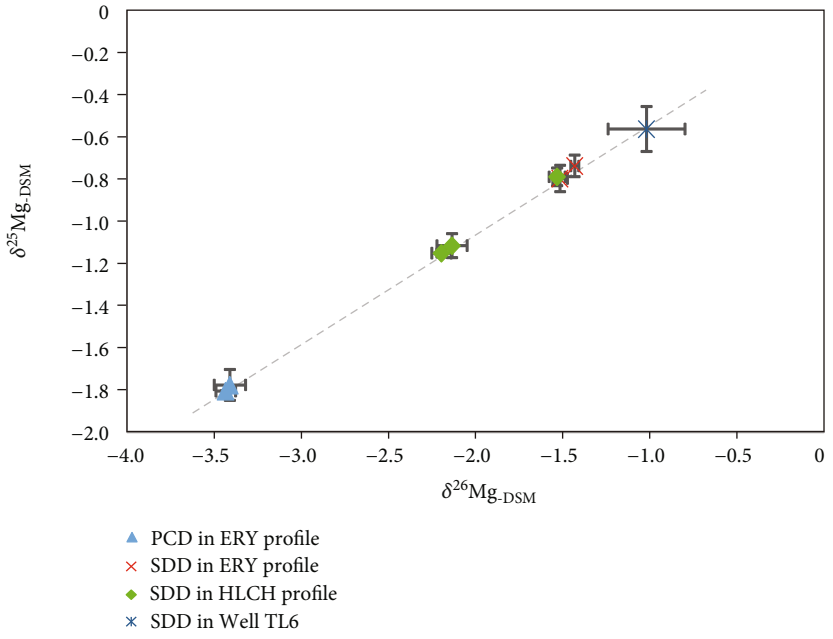

(b)

Figure 8: Continued.

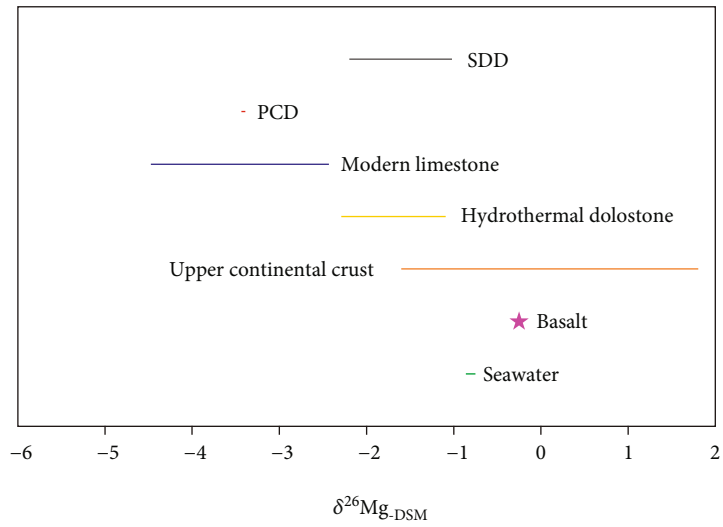

(c)

Figure 8: (a) *In situ* Sr isotope compositions of different dolomite components of the Maokou Formation in Eastern Sichuan. (b) Correlation of $\delta^{25}Mg_{\text{-DSM}}$ and $\delta^{26}Mg_{\text{-DSM}}$ of different dolomite components of the Maokou Formation in Eastern Sichuan. (c) Comparison of Mg isotope compositions. Sr isotope compositions of limestones in the Maokou Formation were cited from Liu et al. [42]. $^{87}Sr/^{86}Sr$ ratios of Permian seawater were from Huang et al. [64]. $\delta^{26}Mg_{\text{-DSM}}$ values of seawater were from Chang et al. [65] and Pearson et al. [66]. $\delta^{26}Mg_{\text{-DSM}}$ values of basalt were cited from Teng et al. [67]. $\delta^{26}Mg_{\text{-DSM}}$ values of upper continental crust were cited from Teng et al. [68]. $\delta^{26}Mg_{\text{-DSM}}$ values of hydrothermal dolostone were from Lavoie et al. [69]. $\delta^{26}Mg_{\text{-DSM}}$ values of modern limestone were cited from Geske et al. [70] and Huang et al. [71].

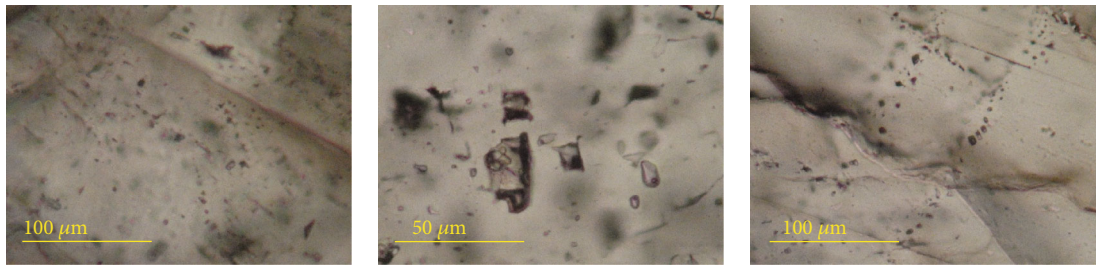

(a) (b) (c)

Figure 9: Fluid inclusions: (a) protogenetic brine inclusions in saddle dolomite, (b) rectangular or elliptical and isolated protogenetic brine inclusions in cloudy-centered dolomite, and (c) isolated protogenetic brine inclusions in coarse-grained calcite.

rectangular or elliptical and have isolated protogenetic brine inclusions with homogenous temperatures of 106.8~169.7°C (Figures 9(c) and 10). Fluid inclusions in SDD have various shapes (Figure 9(a)), such as rectangular, elliptical, and quadrilateral, and belong to isolated protogenetic brine inclusions with homogenous temperatures of 102.7~231.6°C (Figure 10). CGC contains many fluid inclusions, such as quadrilateral, triangular, rectangular, and elliptical, which are isolated protogenetic brine inclusions (Figure 9(c)). The homogenous temperatures of fluid inclusions of many groups in CGC vary from 103.7 to 298.3°C (Figure 10).

5. Discussion

5.1. Dolomitizing Situation. Anomalous degrees of δCe and δEu enable reflecting the redox situation during dolomitizing. Under PAAS normalization, all dolomite components and CGC exhibit negative Ce anomalies (Figure 6(a)). Compared with the limestone in the Maokou Formation, all components and CGC show more intensely negative Ce anomalies, except for CCD (Figure 6(a)). Besides, there is no noticeable Eu anomaly in dolomite components and coarse-crystalline calcites except for SDD and coarse-crystalline calcites in Well TL6 (Figure 6(a)), indicating that they were possibly formed in an open oxidizing environment. However, different dolomite components have different negative Ce anomalies, and the same component also shows varying δCe values (Figure 6(a)), suggesting that the redox condition is constantly changing during the dolomitizing process. CCD has slightly higher δCe values of 0.42~0.48 than CRD and MLD in the ERY profile, inferring that the latter were formed in a stronger oxidizing environment. Likewise, SDD and CGC of the ERY profile have higher δCe values than MLD and CRD, implying that the dolomitizing

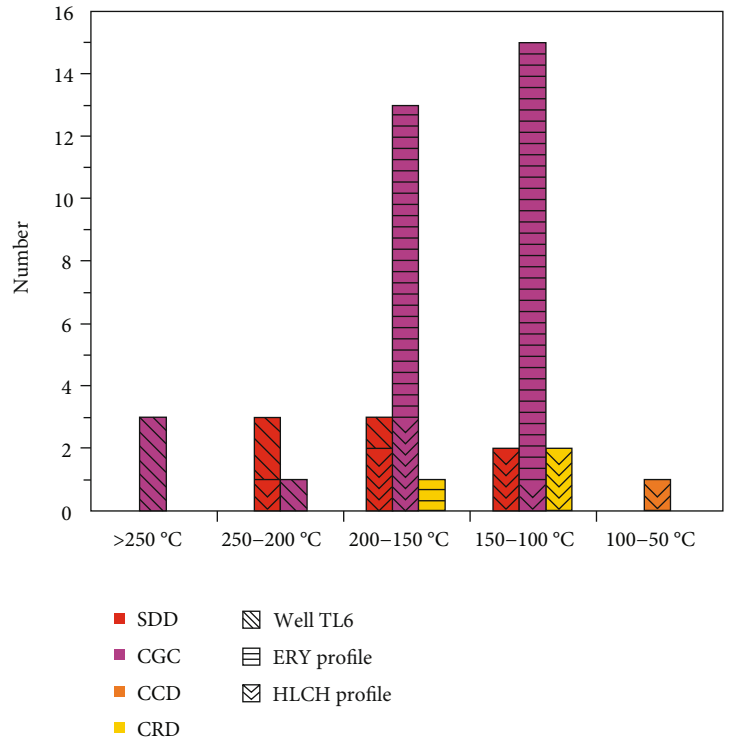

Figure 10: Frequency distribution histogram of homogenous temperatures of fluid inclusions in different dolomite components of the Maokou Formation in Eastern Sichuan.

condition turns to a weaker oxidizing environment. Nevertheless, SDD and CGC have stronger negative Ce anomalies than MLD in the HLCH profile, suggesting that the fluid environment has changed again. And these clues further point out that different profiles have distinct redox environments at the same dolomitizing stage. For instance, MLD of the ERY profile has lower δCe values than that of the HLCH profile, and SDD and CGC of the ERY profile have higher δCe values than those of the HLCH profile, suggesting that there are local differences of redox conditions during dolomitization.

SDD and CGC in Well TL6 have significantly positive Eu and negative Ce anomalies. There are two reasons for the characteristic occurrence: (1) Hydrothermal fluid participated in the dolomitizing process. (2) A closed reducing environment took place. Hydrothermal fluids contain apparently higher ΣREE than seawater and river water and show outstanding positive Eu anomalies, so dolomite and calcite produced from hydrothermal fluids have higher ΣREE than primitive limestones [39, 40]. ΣREE of SDD and CGC in Well TL6 is 5.17-13.17 ppm with an average value of 9.39 ppm, which is higher than ΣREE of the limestone in the Maokou Formation [41] (6.73 ppm). Combined with significantly negative Ce anomalies of SDD and CGC in Well TL6, it is inferred that the obviously positive Eu anomalies may be caused by the participation of hydrothermal fluids. Therefore, SDD and CGC in Well TL6 may be formed in an open oxidizing environment. However, δCe values of PCD (0.95~0.97) in the ERY profile are higher than the limestone in the Maokou Formation [41] (0.84), suggesting a weakly reducing environment.

Na contents can reflect the fluid salinity of a mineral-forming environment. MLD has higher Na contents than SDD and CGC in the HLCH profile (Figure 6(b)), indicating that the former was formed in a high-salinity environment. The ERY profile also has the same characteristics as the HLCH profile (Figure 6(c)). Nonetheless, PCD has lower Na contents than the other components, implying that different dolomite components were formed in distinct salinity environments. SDD and CGC of Well TL6 have the lowest Na contents (Figure 6(c)), probably related to the involvement of hydrothermal fluids.

5.2. Dolomitizing Stages and Sources of Mg^{2+}

5.2.1. The Early Stage. Petrographic observations reveal that PCD, MLD, and CCD show turbid crystal planes (Figures 4(a), 4(c), and 4(e)) and bright orange-red CL (Figures 4(b), 4(d), and 4(f)), whereas CRD and SDD have clean crystal faces and darkly red CL (Figures 4(c), 4(d), 4(g), and 4(h)), indicating that the former and the latter may be products of different fluids. According to the geochemical features, there are similar $^{87}Sr/^{86}Sr$ values among PCD, MLD, CCD, and limestones of the Maokou Formation plotted in the range of Permian seawater [42] (Figure 8(a)), although MgO/CaO and Rb/Sr ratios and Fe+Mn contents of PCD are lower than those of MLD and CCD in the ERY profile (Figures 5(a) and 6(e)). Combined with analogue REE distribution patterns and spider diagrams among PCD, MLD, and CCD (Figures 7(a) and 7(b)), it is inferred that the three may be formed in different periods of the same

fluid. Sr+Ba contents and REE distribution patterns of PCD in the ERY profile are similar to the limestone in the Maokou Formation [41], and the original calcite texture remains in PCD, suggesting that PCD were possibly formed earlier than MLD and CCD.

MgO/CaO values and Al_2O_3 contents of MLD have no obvious variations, different from those of CCD (Figure 5(b)), pointing to internal homogenous compositions of MLD. MLD in the ERY profile has lower Rb/Sr values and Fe+Mn contents than CCD, but it has higher values than PCD (Figure 6(e)). Moreover, MLD in the ERY profile was divided into two groups in terms of Sr contents and Mg/Ca values (Figure 6(g)). The one with high Sr content and low Mg/Ca is similar to PCD, while the other one with low Sr content but high Mg/Ca overlaps with CCD. This evidence supports the inference that PCD, MLD, and CCD of the ERY profile were formed at different periods of the same fluid. In Figure 5(c), the Al_2O_3 contents of CCD gradually decrease from core to rim. The low MgO/CaO values of PCD also correspond to high Al_2O_3 contents (Figure 5(a)). And the protogenetic calcite likewise exhibits the same characteristic (Figure 5(e)), implying that the dolomitizing fluid is attributed to surface fluids. Furthermore, compared with MLD and CCD of the ERY profile, PCD has lower Na contents and higher δCe values, indicating that the dolomitizing situation transforms from the lowly saline and weakly reduced condition to the highly saline and strongly oxidizing condition. Alteration of the Rb/Sr values and Fe+Mn contents among PCD, MLD, and CCD in the ERY profile may be caused by the dolomitizing diagenesis (Figures 6(d) and 6(e)). Wang et al. [43] proposed that the progressively strong metasomatic dolomitization of penecontemporaneous brine will result in Sr contents decreasing and Mn contents increasing in dolomite. Therefore, PCD, MLD, and CCD in the ERY profile were formed in the process of the brine replacing protogenetic calcites. And MLD should be formed earlier than CCD. Cr+Ni contents of PCD, MLD, and CCD show a positive correlation with Rb/Sr ratios in the ERY profile (Figure 6(h)), while their δ^{26}Mg and $^{87}Sr/^{86}Sr$ values do not reflect signals of mantle-derived material (Figures 8(a) and 8(c)). There is no fact for high field strength elements enriching in spider diagrams (Figure 7). These characteristics support that the high-salinity brine is mainly composed of seawater mixing with a few mantle-derived fluids. Compared with MLD of the ERY profile, MLD of the HLCH profile shows higher Rb/Sr ratios and Fe+Mn, Cr+Ni, and Na contents. Although MLD of the HLCH profile has similar REE distribution patterns to the limestone in the Maokou Formation, the spider diagrams show evidently enriched Zr, Hf, and Ti (Figure 7(d)), suggesting that dolomitizing fluids in the HLCH profile may be derived from high-salinity brine with the mixing of more mantle-derived fluids.

5.2.2. The Late Stage. Both CRD and SDD have clean crystal planes and darkly red CL (Figures 4(c), 4(d), 4(g), and 4(h)). CRD of the ERY profile has analogue $^{87}Sr/^{86}Sr$ values similar to SDD of the HLCH profile and Well TL6 (Figure 8(a)), implying that they were generated in the same fluids. CRD contains higher Rb/Sr values and Cr+Ni and Na contents (Figures 6(c) and 6(h)) but lower Fe+Mn contents and δCe values (Figures 6(a) and 6(e)) than those of SDD in the ERY profile. In Figure 7(a), SDD of the ERY profile enriches HREE, different from CRD. Reversely, CRD contains higher Ba, P, Zr, Hf, and Ti contents than SDD in the ERY profile (Figure 7(b)). And $^{87}Sr/^{86}Sr$ values of CRD are higher than CCD in the ERY profile (Figure 8(a)). These facts suppose that CRD of the ERY profile was produced in a mixture of surface fluids and mantle-derived fluids, consistent with high homogenous temperatures of fluid inclusions (Figure 10). The signature that CRD in the ERY profile has high Rb/Sr values and Na contents but low Fe+Mn contents indicates that ΣHREE and δCe values should be inherited from CCD. Also, homogenous temperatures of fluid inclusions of CRD are higher than those of CCD but lower than those of SDD (Figure 10). Because CRD was formed after CCD, the temperature of dolomitizing fluids in the Maokou Formation in Eastern Sichuan should increase progressively. Consequently, SDD was generated after CRD.

SDD shows low Rb/Sr values and Sr contents, which may be associated with the distribution coefficient of Sr in calcite and dolomite. Since the ionic radius of Sr is close to Ca but quite different from Mg, it is generally believed that Sr can replace Ca in calcite or dolomite but cannot substitute Mg in dolomite [44]. In Figures 5(e) and 5(f), CGC contains higher SrO contents than SDD and CRD. Therefore, most of the Sr elements in the fluid enter into the calcite lattice rather than dolomite. SDD has high SrO contents and homogenous temperatures of fluid inclusions and δ^{26}Mg values similar to that of Early Silurian hydrothermal dolomite in southern Quebec, Canada (Figure 8(c)), indicating a hydrothermal dolomitizing model. Likewise, hydrothermal-related minerals in the Maokou Formation, such as pyrite and sphalerite, also support the hydrothermal dolomitization model [24]. Oxygen isotope has the thermal fractionation effect, so the high temperature will cause the δ^{18}O value of calcite and dolomite to become more negative [45]. Chen et al. [46] and Zhang et al. [24] reported that SDD in the Maokou Formation has negative δ^{18}O values ranging from -6.9‰ to -7.6‰, indicating that SDD is indeed affected by hydrothermal fluids. CRD shows similar REE distribution patterns to SDD in the ERY profile (Figure 7(a)), although they both have several geochemical differences. CRD of the ERY profile has similar $^{87}Sr/^{86}Sr$ values to that of SDD of the HLCH profile and Well TL6 (Figure 8(a)). This evidence indicates that magmatic fluids do not change chemical compositions but only improve the temperature. Hydrothermal fluids forming SDD may be mixed with more surface water, which results in a reduction of the Cr+Ni contents and an increase of the Fe+Mn contents of SDD. Besides, Lottermoser [47] argued that ΣREE of minerals crystallizing from fluids predominantly depends on ΣREE of the fluid. Thus, SDD in Well TL6 exhibits distinctive positive Eu anomalies (Figure 6(a)) which are possibly related to the type of rocks through which surface water flows. As mentioned above, two phases of intersecting carbonate veins can be observed in the field (Figure 3(i)), but SDD or CGC does not show significant geochemical and isotopic differences. Hence, CRD and two phases of carbonate veins may be generated at

different periods of contemporaneous hydrothermal fluids, analogue to multipulsing Mg^{2+} metasomatism during the ascent of mantle-derived fluids [48].

5.3. Dolomitizing Time. Residual hydrocarbons filling in pores between MLD and SDD and fractures can be observed in dolostones or calcareous dolostones of the Maokou Formation in Eastern Sichuan (Figure 3(j)), suggesting that oil and gas filling occurred later after the formation of SDD. Jiang et al. [49] proposed that source rocks of the Maokou Formation had produced plenty of hydrocarbons in Middle-Late Triassic via recovering the burial history of Well GC2. So, the dolomitizing time of the Maokou Formation was at least earlier than Middle-Late Triassic. Petrographic observations show that carbonate veins filled in the fractures (Figure 3(h)), testifying that SDD, one of the components of carbonate veins, has to crystallize before the fractures. The seismic profile of Well GC2 revealed that tensile basement faults disappeared in coarse-grained dolostones in the Upper Permian Wujiaping Formation [46]. Liu et al. [50] reported that the Huayingshan fault zone is a regional basement fault formed in the Proterozoic Jinning Stage and was reactivated in the Late Permian Dongwu Stage induced by the basalt eruption in the middle of the Huayingshan structure. Therefore, SDD in carbonate veins should be formed after Late Permian. CRD is also of hydrothermal origin but is not distributed in the cracks. Combined with homogenous temperatures of fluid inclusions slightly lower than those of SDD, the formation time of CRD is the same as SDD. Moreover, the Emei taphrogeny occurred after the deposition of the Maokou Formation according to previous studies [34–37], which caused generating the supergene karst system on top of the Maokou Formation. Hence, the late stage of dolomitization in the Maokou Formation took place synchronous with or later than the karst system, because SDD exists by filling in the pores or cracks.

The textural relationship that CRD envelops CCD supports that PCD, MLD, and CCD were formed before CRD and SDD (Figure 4(c)). Additionally, PCD, MLD, and CCD are distributed in the matrix and are relevant with the high-salinity brine, implying that they were produced before the fractures. According to the paleotemperature gradient profile of Sichuan Basin established by Wang et al. [51], the paleotemperature gradient is 3.53°C/hm in Eastern Sichuan during Late Permian-Early Triassic. The Maokou Formation was situated in the buried depth of 930 m when CCD had been generated by assuming that the surface temperature was 25°C. At present, it is generally considered that the burial depth ranging from 500 to 1000 m is a shallow burial stage [52]. Consequently, PCD, MLD, and CCD were formed in the shallow burial stage of the Maokou Formation earlier than Late Permian. Hao et al. [53] reported that the early stage of dolomitization in the Maokou Formation happened at least 257 Ma via U-Pb isotope dating, compatible with the above inference and earlier than the exposure period of the Maokou Formation.

5.4. Dolomitizing Model. In the past 30 years, many scholars have proposed a variety of dolomitizing models for the genesis of dolostones in the Maokou Formation in Sichuan Basin, including the burial model [27], the mixed-water model [28], the basalt-leaching model [54], the hot-water model [29–31], and the tectonic hydrothermal model [24, 42, 45, 46, 55]. However, the dolomitizing model of the Maokou Formation in different regions of Sichuan Basin may be various. As for the Maokou Formation in Eastern Sichuan, the hot-water model proposed by Wang et al. [29] and Li et al. [30] lacks sufficient evidence. For example, it is unreasonable that the hot-water model was considered only based on SDD, positive Eu anomalies, and a $Fe - Mn - (Cu + Ni + Co) \times 10$ triangular discriminant diagram. First, hydrothermal dolomites also have these signatures [24, 42, 45]. Second, PCD and MLD do not have these characteristics in this study.

As mentioned above, PCD, MLD, and CCD of the Maokou Formation in Eastern Sichuan were formed in the shallow burial stage before Late Permian. PCD is the main component of fine-grained dolostones of Member 1 and Member 2, while MLD and CCD are mainly distributed in the middle–coarse-grained dolostones of Member 3, indicating that at the shallowly buried stage, the lower layer of Maokou Formation was less dolomitized, but the upper layer was stronger. These features support that dolomitizing fluids should originate from the surface rather than the underground. Hence, we think that PCD, MLD, and CCD were formed at different stages of dolomitizing high-salinity brines, and high-salinity brines were principally derived from closed seawater mixing with little mantle-derived fluids. The seawater primarily migrated along pores, and the mantle-derived fluid may predominately seep upward via microcracks and pores (Figure 11(a)).

CRD and SDD have obvious hydrothermal characteristics and enrich high field strength elements Nb, Zr, Hf, and Ti and compatible elements Cr and Ni (Figures 6(h) and 7) with high homogenous temperatures of fluid inclusions (Figure 10). Furthermore, Emeishan basalts are exposed locally on the top of the Maokou Formation [56]. Therefore, we speculate that hydrothermal fluids may be related to the Emei mantle plume simultaneously. Nowadays, it is generally believed that the Emei mantle plume had a large-scale thermal effect [57]. Zhu et al. [58] reported that the heat flow value of strata in Sichuan Basin slowly increased from 290 Ma (Hercynian) and reached a maximum in ca. 259 Ma; then, it was reduced to the current temperature gradient until 230 Ma. Moreover, Sichuan Basin was in a tensional environment and developed lots of basement faults with the characteristics of high angle, short distance, large scale, and long extension [59–61]. There is a NE-SW trending Huayingshan fault zone and many NW-SE trending basement faults in Eastern Sichuan [23]. The Huayingshan fault zone is a large-scale basement fault in the Proterozoic Jinning Stage and was reactivated to result in the basaltic eruption around the Huayingshan structural axis in the Late Permian Dongwu Stage [50], identical to observations of basalt outcropped locally on the top of the Maokou Formation in Eastern Sichuan [56]. Davies and Smith [9] pointed out that hydrothermal fluid activities are specially developed in specific structures such as extensional faults, deep and

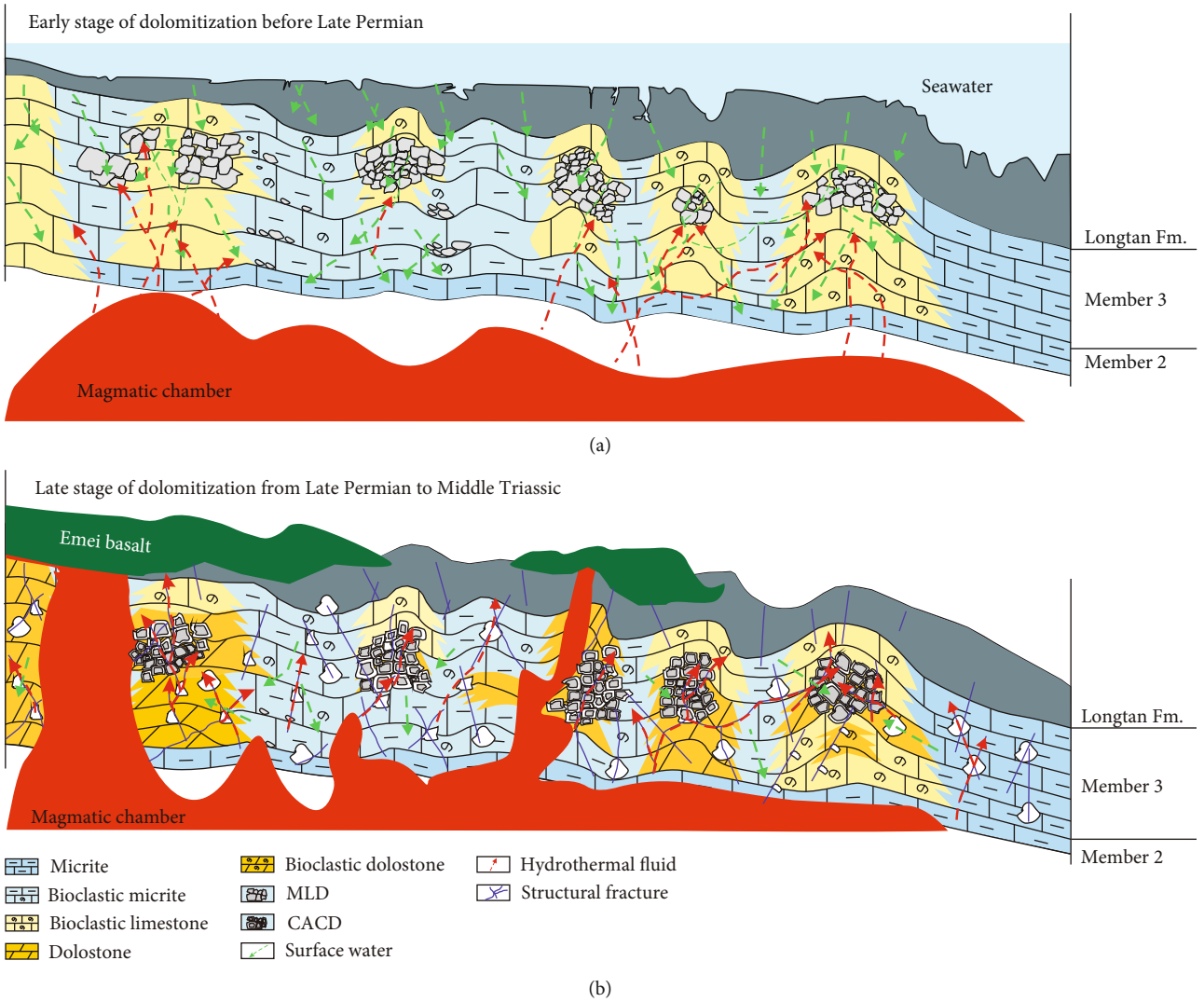

Figure 11: Dolomitizing model of the Middle Permian Maokou Formation in Eastern Sichuan. MLD: mosaic-like dolomite. CACD: clear-rimmed dolomite.

large strike-slip faults, tensional faults, torsional faults, and intersections of deep and large strike-slip faults. Thus, the fracture system provides an important channel for hydrothermal fluids in Eastern Sichuan and is the first choice for large-scale upward migration of Mg-rich fluids (Figure 11(b)). These speculations enable understanding the high homogenous temperatures of high-fluid inclusions and carbonate veins filling in fractures.

Consequently, dolostones in Maokou Formation in Eastern Sichuan were mainly formed by two stages of dolomitizing fluids. The early stage was high-salinity brine which mainly migrated along pores. The late stage was relevant to the activity of the Emei mantle plume and belonged to hydrothermal fluids which primarily migrated upward along structural fractures or faults and filled in structural fractures.

6. Conclusions

In this study, the integration of multiple field profiles, *in situ* geochemistry, Sr-Mg isotopes, and fluid inclusions was carried to discuss the dolomitizing process and lateral differences of Middle Permian Maokou Formation in Eastern Sichuan. According to textural signatures, dolomites were subdivided into four components: partially clouded dolomite (PCD), mosaic-like dolomite (MLD), cloudy-centered and clear-rimmed dolomite (CACD), and saddle dolomite (SDD). Their *in situ* geochemical differences are essential to distinguish the genesis of dolomites. The conclusions can be summarized as follows:

(1) PCD, MLD, and cloudy-centered dolomite (CCD) were formed during the early dolomitization in terms of similar textural and geochemical features. They all show turbid crystal planes and bright orange-red CL and have similar $^{87}Sr/^{86}Sr$ ratios and rare-earth patterns. Dolomitization of the early stage happened via high-salinity brines with a mixture of seawater and little mantle-derived fluids replacing protogenetic calcites which mainly migrated along pores in the shallow burial stage before Late Permian.

However, the high-salinity brine in the ERY profile consists of mixing seawater and a little mantle-derived fluid. The HLCH profile might undergo mixing high-salinity brine and more mantle-derived fluid and the more intensely diagenetic process

(2) CRD and SDD were formed in the late stage of dolomitization. They all have clean crystal planes and darkly red CL. SDD contains slightly lower Cr and Ni contents and slightly higher Fe and Mn contents than those of CRD, and its δ^{26}Mg values are analogous to Early Silurian hydrothermal dolomite in southern Quebec, Canada. Combined with high SrO contents and homogenous temperatures of fluid inclusions of CRD and SDD, they were generated by hydrothermal dolomitization. Dolomitizing fluids mainly migrating along structural fractures or faults and filling in structural fractures occurring from Late Permian to Middle-Late Triassic are hydrothermal fluids which are associated with activities of the Emei mantle plume and composed of a mixture of magmatic fluids and surface water

Data Availability

The data used to support the findings of this study are included within the article.

Conflicts of Interest

The authors declare that they have no conflicts of interest.

Acknowledgments

The authors gratefully thank the Sinopec Exploration Company for providing core samples and geological data. This study was jointly supported by the National Natural Science Foundation of China (Grant numbers 42072140, 41672113, and 41902153), the Chongqing Natural Science Foundation of China (Grant numbers cstc2020jcyj and msxmX0217), and the Foundation of Chongqing Education Commission (Grant number KJQN202001517).

References

[1] H. G. Machel, "Concepts and models of dolomitization: a critical reappraisal," *Geological Society, London, Special Publications*, vol. 235, no. 1, pp. 7–63, 2004.

[2] I. Friedman and J. E. Sanders, "Origin and occurrence of dolostone," in *Carbonate Rocks*, G. V. Chilingar, H. J. Bissel, and R. W. Fairbridge, Eds., pp. 267–348, Elsevier, Amsterdam, 1967.

[3] K. J. Hsu and J. Schneider, "Progress report on dolomitization—hydrology of Abu Dhabi Sabkhas, Arabian Gulf," in *The Persian Gulf*, pp. 409–422, Springer, 1973.

[4] J. E. Adams and M. L. Rhodes, "Dolomitization by seepage refluxion," *AAPG Bulletin*, vol. 44, pp. 1912–1920, 1960.

[5] K. Badiozamani, "The Dorag dolomitization model—application to the Middle Ordovician of Wisconsin," *SEPM Journal of Sedimentary Research*, vol. 43, no. 4, pp. 965–984, 1973.

[6] P. A. Baker and M. Kastner, "Constraints on the formation of sedimentary dolomite," *Science*, vol. 213, no. 4504, pp. 214–216, 1981.

[7] C. Vasconcelos, J. A. McKenzie, S. Bernasconi, D. Grujic, and A. J. Tiens, "Microbial mediation as a possible mechanism for natural dolomite formation at low temperatures," *Nature*, vol. 377, no. 6546, pp. 220–222, 1995.

[8] D. Chen, H. Qing, and C. Yang, "Multistage hydrothermal dolomites in the middle Devonian (Givetian) carbonates from the Guilin area, South China," *Sedimentology*, vol. 51, no. 5, pp. 1029–1051, 2004.

[9] G. R. Davies and L. B. Smith Jr., "Structurally controlled hydrothermal dolomite reservoir facies: an overview," *AAPG Bulletin*, vol. 90, no. 11, pp. 1641–1690, 2006.

[10] E. Azomani, K. Azmy, N. Blamey, U. Brand, and I. al-Aasm, "Origin of Lower Ordovician dolomites in eastern Laurentia: controls on porosity and implications from geochemistry," *Marine and Petroleum Geology*, vol. 40, pp. 99–114, 2013.

[11] J. Niu, W. H. Huang, and F. Liang, "Geochemical characteristics and genesis of Lower Ordovician dolomite in the southwest Tarim Basin, Northwest China," *Episodes*, vol. 42, no. 1, pp. 33–54, 2019.

[12] J. M. Gregg and K. L. Shelton, "Dolomitization and dolomite neomorphism in the back reef facies of the Bonneterre and Davis formations (Cambrian), southeastern Missouri," *SEPM Journal of Sedimentary Research*, vol. 60, no. 4, pp. 549–562, 1990.

[13] I. S. Al-Aasm and J. J. Packard, "Stabilization of early-formed dolomite: a tale of divergence from two Mississippian dolomites," *Sedimentary Geology*, vol. 131, no. 3-4, pp. 97–108, 2000.

[14] M. Liu, Y. Xiong, C. Xiong et al., "Evolution of diagenetic system and its controls on the reservoir quality of pre-salt dolostone: the case of the Lower Ordovician Majiagou Formation in the central Ordos Basin, China," *Marine and Petroleum Geology*, vol. 122, p. 104674, 2020.

[15] L. A. Derry, M. D. Brasier, R. M. Corfield, A. Y. Rozanov, and A. Y. Zhuravlev, "Sr and C isotopes in Lower Cambrian carbonates from the Siberian craton: a paleoenvironmental record during the "Cambrian explosion"," *Earth and Planetary Science Letters*, vol. 128, no. 3-4, pp. 671–681, 1994.

[16] L. A. Derry, L. S. Keto, S. B. Jacobsen, A. H. Knoll, and K. Swett, "Sr isotopic variations in upper proterozoic carbonates from Svalbard and East Greenland," *Geochimica et Cosmochimica Acta*, vol. 53, no. 9, pp. 2331–2339, 1989.

[17] S. J. Huang, "A study on carbon and strontium isotopes of late Paleozoic carbonate rocks in the upper Yangtze platform," *Acta Geologica Sinica*, vol. 71, no. 1, pp. 45–53, 1997.

[18] N. P. James and P. W. Choquette, "Diagenesis 9. Limestones—the meteoric diagenetic environment," *Geoscience Canada*, vol. 11, no. 4, pp. 162–194, 1984.

[19] D. W. Morrow, "Diagenesis I. Dolomite—part I. The chemistry of dolomitization and dolomite precipitation," *Geosciences Canada*, vol. 9, pp. 5–13, 1982.

[20] U. Brand and J. Veizer, "Chemical diagenesis of a multicomponent carbonate system—1. Trace elements," *SEPM Journal of Sedimentary Research*, vol. 50, no. 4, pp. 1219–1236, 1980.

[21] L. Zhu, Z. Wang, Q. Feng, B. Zhang, L. Wei, and Z. Yu, "Genesis of dolomite in the upper assemblage of the Ordovician Majiagou Formation in the southeastern Sulige gas field, Ordos Basin, China: evidence from C, O, and Sr isotopes and

major and trace elements," *Energy Exploration & Exploitation*, vol. 38, no. 6, pp. 2729–2751, 2020.

[22] R. Jia and D. Liu, "The relationship between dolomitization and organic matter occurrence in Lower Paleozoic carbonate in the Ordos Basin," *Chinese Science Bulletin*, vol. 45, no. S1, pp. 41–46, 2000.

[23] D. Hu, L. Wang, R. Huang, J. Duan, Z. Xu, and L. Pan, "Characteristics and main controlling factors of the Middle Permian Maokou dolomite reservoirs in the eastern Sichuan Basin," *Natural Gas Industry*, vol. 39, no. 6, pp. 13–21, 2019.

[24] T. Zhang, J. Lin, Y. Han, Z. Wang, J. Qin, and R. Zhang, "Pattern of hydrothermal dolomitization in the Middle Permian Maokou Formation, eastern Sichuan Basin, and its alteration on reservoirs herein," *Oil & Gas Geology*, vol. 41, no. 1, pp. 132–143, 2020.

[25] X. Tang, X. Tan, H. Liu et al., "Characteristics and development mechanism of dolomite and dolomitic quartzite reservoirs of the Middle Permian Maokou Formation in eastern Sichuan Basin," *Oil & Gas Geology*, vol. 37, no. 5, pp. 731–743, 2016.

[26] D. Li, H. Chen, H. Chen et al., "Relationship between reservoir development in the Middle Permian Maokou Formation and paleostructure evolution in the Sichuan Basin," *Oil & Gas Geology*, vol. 37, no. 5, pp. 756–763, 2016.

[27] Y. He and Z. Feng, "Origin of fine- to coarse-grained dolostones of Lower Permian in Sichuan Basin and its peripheral regions," *Journal of Jianghan Petroleum Institute*, vol. 4, no. 18, pp. 15–20, 1996.

[28] Y. Zhang, "Dolomitization in Permian rocks in Sichuan Basin," *Acta Petrolei Sinica*, vol. 3, no. 1, pp. 29–33, 1982.

[29] H. Wang, H. Shen, D. Huang et al., "Origin and distribution of hydrothermal dolomites of the Middle Permian in the Sichuan Basin," *Natural Gas Industry*, vol. 34, no. 9, pp. 25–32, 2014.

[30] Y. Li, H. Shen, X. Shi, H. Wang, S. Chen, and X. Yuan, "Distribution and origin of dolomites in Maokou Formation, Eastern and Central Sichuan Basin," *Natural Gas Exploration & Development*, vol. 36, no. 4, pp. 1–3, 2013.

[31] G. Yang, H. Wang, H. Shen et al., "Characteristics and exploration prospects of Middle Permian reservoirs in the Sichuan Basin," *Natural Gas Industry*, vol. 35, no. 7, pp. 10–16, 2015.

[32] K. Zhang, C. Jia, Y. Song et al., "Analysis of Lower Cambrian shale gas composition, source and accumulation pattern in different tectonic backgrounds: a case study of Weiyuan Block in the Upper Yangtze region and Xiuwu Basin in the Lower Yangtze region," *Fuel*, vol. 263, article 115978, 2020.

[33] Z. Luo, "New recognition of basement in Sichuan Basin," *Journal of Chengdu University of Technology*, vol. 25, no. 2, pp. 191–200, 1998.

[34] S. Liu, B. Deng, Z. Li, and W. Sun, "The texture of sedimentary basin-orogenic belt system and its influence on oil/gas distribution," *Acta Petrologica Sinica*, vol. 27, no. 3, pp. 621–635, 2011.

[35] Y. B. Zhang, "Sequence stratigraphy and depositional models of the Middle Permian in Sichuan Basin," Chengdu University of Technology: PhD thesis, 2011.

[36] Y. Wang and Y. Jin, "The formation of dolomite and paleokarst of the Lower Permian series in Sichuan Basin and the relation to the Emei taphrogenesis," *Journal of Chengdu University of Technology*, vol. 24, no. 1, pp. 12–20, 1997.

[37] J. Su, S. Zhang, H. Yang, G. Zhu, J. Chen, and B. Zhang, "Control of fault system to formation of effective carbonate reservoir and the rules of petroleum accumulation," *Acta Petrolei Sinica*, vol. 31, no. 2, pp. 196–203, 2010.

[38] H. Yuan, "State Key Laboratory of Continental Dynamics, Northwest University," *Rock and Mineral Analysis*, vol. 31, no. 6, pp. 1090–1092, 2012.

[39] A. Michard, F. Albarède, G. Michard, J. F. Minster, and J. L. Charlou, "Rare-earth elements and uranium in high-temperature solutions from East Pacific Rise hydrothermal vent field (13°N)," *Nature*, vol. 303, no. 5920, pp. 795–797, 1983.

[40] A. Michard and F. Albarede, "The REE content of some hydrothermal fluids," *Chemical Geology*, vol. 55, no. 1-2, pp. 51–60, 1986.

[41] Q. Li, S. Xu, H. Chen et al., "Geochemical characteristics and palaeo-environmental implication of Middle Permian Maokou Formation in Wangcang region, Sichuan Basin, China," *Journal of Chengdu University of Technology*, vol. 45, no. 3, pp. 268–281, 2018.

[42] H. Liu, T. Ma, X. Tan et al., "Origin of structurally controlled hydrothermal dolomite in epigenetic karst system during shallow burial: an example from Middle Permian Maokou Formation, central Sichuan Basin, SW China," *Petroleum Exploration and Development*, vol. 43, no. 6, pp. 1000–1012, 2016.

[43] L. Wang, W. Hu, X. Wang et al., "Variation of Sr content and $^{87}Sr/^{86}Sr$ isotope fractionation during dolomitization and their implications," *Oil & Gas Geology*, vol. 37, no. 4, pp. 464–472, 2016.

[44] Z. Li, E. Xu, M. Fan et al., "Geochemical characteristics and formation of dolostones from the Changxing Formation at Puguang gas field in Sichuan Basin," *Geochimica*, vol. 39, no. 4, pp. 371–380, 2010.

[45] J. Wang, Y. Gu, Y. Tao, Z. Qiang, S. Qiang, and C. Jiang, "The model of dolomitization jointly controlled by two-episode fluids in Maokou Formation in Central Sichuan Basin," *Acta Sedimentologica Sinica*, vol. 34, no. 2, pp. 236–249, 2016.

[46] X. Chen, W. Zhao, L. Zhang et al., "Discovery and exploration significance of structure-controlled hydrothermal dolomites in the Middle Permian of the central Sichuan Basin," *Acta Petrolei Sinica*, vol. 33, no. 4, pp. 562–569, 2012.

[47] B. G. Lottermoser, "Rare earth elements and hydrothermal ore formation processes," *Ore Geology Reviews*, vol. 7, no. 1, pp. 25–41, 1992.

[48] Y. He, B. Liu, and S. Qin, "Study on the dolomitization and dolostone genesis," *Acta Scientiarum Naturalium Universitatis Pekinensis*, vol. 46, no. 6, pp. 1010–1020, 2010.

[49] Q. Jiang, S. Hu, Z. Wang, T. Wang, Q. Li, and X. Zhai, "Genesis of medium-macro-crystalline dolomite in the Middle Permian of Sichuan Basin," *Oil & Gas Geology*, vol. 35, no. 4, pp. 503–510, 2014.

[50] H. Liu, Z. Sun, Z. Li et al., "Syndepositional tectonic activities in the Huayingshan fracture belt during the Triassic Jialing River phase and its implication on sedimentation and reservoir development," *Journal of Stratigraphy*, vol. 34, no. 3, pp. 312–320, 2010.

[51] Y. Wang, X. Yu, Y. Yang, and J. Zhang, "Applications of fluid inclusions in the study of paleo-geotemperature in Sichuan Basin," *Earth Science - Journal of China University of Geosciences*, vol. 23, no. 3, pp. 69–72, 1998.

[52] S. N. Ehrenberg, O. Walderhaug, and K. Bjørlykke, "Carbonate porosity creation by mesogenetic dissolution: reality or illusion?," *AAPG Bulletin*, vol. 96, no. 2, pp. 217–233, 2012.

[53] Y. Hao, Q. Y. Yao, H. Tian, M. F. Gu, M. She, and Y. Wang, "Sedimentary characteristics and reservoir-controlling factors of the Permian Maokou Formation in Sichuan Basin," *Marine Origin Petroleum Geology*, vol. 25, no. 3, pp. 202–209, 2020.

[54] Z. Jin and Z. Feng, "Origin of Dolostones of the Lower Permian in East Yunnan-West Sichuan: dolomitization through leaching of basalts," *Acta Sedimentologica Sinica*, vol. 17, no. 3, pp. 383–389, 1999.

[55] Y. Jiang, Y. Gu, K. Li, S. Li, M. Luo, and B. He, "Space types and origins of hydrothermal dolomite reservoirs in the Middle Permian strata, Central Sichuan Basin," *Natural Gas Industry*, vol. 38, no. 2, pp. 16–24, 2018.

[56] J. Liu, H. Zheng, B. Liu et al., "Petrology and geochemical characteristics of dolomite in the Middle Permian Maoukou Formation, central Sichuan," *Petroleum Research*, vol. 2, no. 4, pp. 366–377, 2017.

[57] C. Zhang, J. Liu, X. Liu, Z. Yang, Y. Li, and D. Wu, "Primary discussion on ore-forming effect of Emei Igneous Province," *Mineralogy and Petrology*, vol. 24, no. 1, pp. 5–9, 2004.

[58] C. Zhu, M. Xu, Y. Yuan et al., "Palaeo-geothermal response and record of the effusing of Emeishan basalts in Sichuan basin," *Chinese Science Bulletin*, vol. 6, no. 55, pp. 474–482, 2010.

[59] Z. Li, M. Pan, D. Xiao, G. Chen, Z. Lu, and D. Ying, "Studies of extension-compression tectonic dynamic setting in Sichuan Basin," *Acta Scientiarum Naturalium Universitatis Pekinensis*, vol. 37, no. 1, pp. 87–93, 2001.

[60] W. Li, J. Liu, S. Deng, B. Zhang, and H. Zhou, "The nature and role of Late Sinian-Early Cambrian tectonic movement in Sichuan Basin and its adjacent areas," *Acta Petrolei Sinica*, vol. 36, no. 5, pp. 546–556, 2015.

[61] J. Yin, Z. Gu, and Q. Li, "Characteristics of deep-rooted faults and their geological significances in Dachuanzhong area, Sichuan Basin," *Oil & Gas Geology*, vol. 34, no. 3, pp. 376–382, 2013.

[62] S. M. McLennan, "Rare earth elements in sedimentary rocks: influence of provenance and sedimentary processes," *Geochemistry and Mineralogy of Rare Earth Elements, Reviews in Mineralogy*, vol. 21, pp. 169–200, 1989.

[63] R. L. Rudnick and S. Gao, "Composition of the continental crust," *The Crust*, vol. 3, pp. 1–64, 2003.

[64] S. J. Huang, Y. Huang, Y. F. Lan, and K. K. Huang, "A comparative study on strontium isotope composition of dolomites and their coeval seawater in the Late Permain-Early Triassic, NE Sichuan basin," *Acta Petrologica Sinica*, vol. 27, no. 12, pp. 3831–3842, 2011.

[65] V. T. C. Chang, A. Makishima, N. S. Belshaw, and R. K. O'Nions, "Purification of Mg from low-Mg biogenic carbonates for isotope ratio determination using multiple collector ICP-MS," *Journal of Analytical Atomic Spectrometry*, vol. 18, no. 4, pp. 296–301, 2003.

[66] N. J. Pearson, W. L. Griffin, O. Alard, and S. Y. O'Reilly, "The isotopic composition of magnesium in mantle olivine: records of depletion and metasomatism," *Chemical Geology*, vol. 226, no. 3-4, pp. 115–133, 2006.

[67] F. Z. Teng, W. Y. Li, S. Ke et al., "Magnesium isotopic composition of the Earth and chondrites," *Geochimica et Cosmochimica Acta*, vol. 74, no. 14, pp. 4150–4166, 2010.

[68] F. Z. Teng, "Magnesium isotope geochemistry," *Reviews in Mineralogy and Geochemistry*, vol. 82, no. 1, pp. 219–287, 2017.

[69] D. Lavoie, S. Jackson, and I. Girard, "Magnesium isotopes in high-temperature saddle dolomite cements in the Lower Paleozoic of Canada," *Sedimentary Geology*, vol. 305, pp. 58–68, 2014.

[70] A. Geske, R. H. Goldstein, V. Mavromatis et al., "The magnesium isotope (δ^{26}Mg) signature of dolomites," *Geochimica et Cosmochimica Acta*, vol. 149, pp. 131–151, 2015.

[71] K. J. Huang, B. Shen, X. G. Lang et al., "Magnesium isotopic compositions of the Mesoproterozoic dolostones: implications for Mg isotopic systematics of marine carbonates," *Geochimica et Cosmochimica Acta*, vol. 164, pp. 333–351, 2015.